

Analog Quantum Simulation of Coupled Electron-Nuclear Dynamics in Molecules

Jong-Kwon Ha¹ and Ryan J. MacDonell^{1, 2, *}

¹*Department of Chemistry, Dalhousie University,
6243 Alumni Cres, Halifax, NS B3H 4R2, Canada*

²*Department of Physics and Atmospheric Science, Dalhousie University,
1453 Lord Dalhousie Dr, Halifax, NS B3H 4R2, Canada*

(Dated: September 9, 2024)

Understanding the coupled electron-nuclear dynamics in molecules induced by light-matter interactions is crucial for potential applications of photochemical processes, but it is challenging due to the high computational costs of exact quantum dynamics simulations. Quantum computing has the potential to reduce the computational cost required for exact quantum dynamics simulations by exploiting the quantum nature of the computational device. However, existing quantum algorithms for coupled electron-nuclear dynamics simulation either require fault-tolerant devices, or use the Born-Oppenheimer (BO) approximation and a truncation of the electronic basis. In this work, we present the first analog quantum simulation approach for molecular vibronic dynamics in a pre-BO framework, i.e. without the separation of electrons and nuclei, by mapping the molecular Hamiltonian to a device with coupled qubits and bosonic modes. We show that our approach has exponential savings in resource and computational costs compared to the equivalent classical algorithms. The computational cost of our approach is also exponentially lower than existing BO-based quantum algorithms. Furthermore, our approach has a much smaller resource scaling than the existing pre-BO quantum algorithms for chemical dynamics. The low cost of our approach will enable an exact treatment of electron-nuclear dynamics on near-term quantum devices.

I. INTRODUCTION

Light-matter interactions are the source of many phenomena in molecular systems such as vision [1–3], photosynthesis [4–7], photovoltaics [8–11], and photocatalysis [12, 13]. In order to apply light-matter interactions to the development of high-functional molecular devices, it is important to understand their underlying mechanisms. In principle, the molecular time-dependent Schrödinger equation can be exactly solved for a system of electrons and nuclei to simulate molecular dynamics. However, it is practically impossible for molecules with more than a few atoms due to the exponential scaling of its computational cost with respect to system size.

The Born-Oppenheimer (BO) approximation neglects the coupling between electronic and nuclear degrees of freedom, known as nonadiabatic coupling (NAC) [14]. Molecular dynamics within in the BO approximation are reduced to nuclear dynamics on a single BO state, i.e. on an eigenstate of electronic Hamiltonian. Although the BO approximation has been successfully applied to study ground-state chemical reactions, it fails to describe light-induced chemical reactions where the molecule can reach strong NAC regions after photo-excitation of the molecular electronic state [14]. The BO approximation can be extended to the group BO approximation (GBOA), which takes into account NACs between a group of BO states considered to be relevant to the dynamics, while NACs to states outside of the group are neglected [14]. The molecular dynamics are then described as nuclear

dynamics on multiple BO potential energy surfaces coupled via NACs. The majority of existing simulation methods make use of the GBOA since it extends the scope of molecular dynamics simulation while using conventional electronic structure methods [15–17]. However, the GBOA can lead to the wrong description of molecular dynamics due to the truncation of the electronic basis set to a small number of BO states. Furthermore, since existing simulation methods with the GBOA require an accurate calculation of BO states and their gradients (including NACs), the computational cost for accurate simulations can become intractable.

Pre-Born-Oppenheimer (pre-BO) methods, on the other hand, naturally include nonadiabatic effects since they treat nuclei and electrons without separation [18–24]. There have been many studies on the pre-BO theory with both first quantization [18–21] and second quantization [22–24] of the molecular Hamiltonian. One well-known approach using the pre-BO framework is the nuclear-electronic orbital (NEO) method which treats certain nuclei as quantum particles using a basis of nuclear orbitals [22]. Recently, an approach based on the multi-configurational time-dependent Hartree method using a second quantization representation of electronic degrees of freedom was developed, which enables the description of coupled electron-nuclear dynamics without electronic potential energy surfaces [24]. Nevertheless, the development of methods in the pre-BO framework is still far behind the methods in the BO framework since the computational cost of a pre-BO treatment of molecular dynamics is much greater.

Quantum computing can significantly reduce the computational cost of the simulation of quantum mechanical systems by exploiting the intrinsic quantum nature of the

* rymac@dal.ca

computational device [25–28]. Most near-term quantum computing research in the field of quantum chemistry is based on the variational quantum eigensolver (VQE) method [29–33]. VQE and similar methods typically use the BO approximation to obtain electronic properties at fixed classical nuclear configurations. Although there are several quantum algorithms for chemical dynamics without the BO approximation [34–36], most methods still adopt the GBOA for near-term applications with variational quantum algorithms [37, 38] or analog mappings [39–41]. There have been proposals for near-term pre-BO eigenvalue optimization on quantum computers using NEO and VQE [42], as well as proposals for time-dependent algorithms with a real-space, first quantized wavefunction ansatz for electrons and nuclei on fault-tolerant quantum computers [34, 36]. The intractability of quantum dynamics simulations with a pre-BO wavefunction on classical computers suggests that a pre-BO quantum simulation could show an earlier quantum advantage than methods using the BO framework. Therefore, it is desirable to develop near-term, pre-BO quantum algorithms with scaling advantages in quantum resource and operations over existing methods for chemical dynamics.

In this work, we propose the first analog quantum simulation method for molecular vibronic dynamics in the pre-BO framework. Our approach maps the second quantized pre-BO representation of the molecular vibronic Hamiltonian onto an analog quantum device, and thus treats the electron-nuclear interactions exactly. Specifically, we map the nuclear vibrational motions to bosonic modes of a device and use a fermion-qubit mapping for electronic degrees of freedom. We show that our method can efficiently simulate the exact molecular vibronic dynamics within a given single-particle basis set, and therefore it is suitable for accurate near-term quantum simulations of coupled electron-nuclear dynamics. As an example, we show how a single-mode vibronic model system could be simulated on an trapped ion quantum computer on the scale of current devices. Finally, we show how the scaling of our approach out-performs all previous approaches in terms of hardware resources, implementation cost, and classical pre-calculation.

II. THEORY

Our simulation approach is restricted to vibronic (vibrational + electronic) internal degrees of freedom of the molecule, meaning the translational and rotational degrees of freedom of the atomic nuclear coordinates are removed. In general, this can be achieved by any unitary transformation of the Cartesian atomic coordinates that separates the 6 collective translations and rotations of the molecule, given by vectors $\mathbf{Q}_{\text{trans}}$ and \mathbf{Q}_{rot} , from the $3N_{\text{at}} - 6$ vibrational internal coordinates, $\mathbf{Q} \equiv \mathbf{Q}_{\text{vib}}$. For the remainder of the manuscript, we assume that mass-weighted normal mode coordinates are used, whereby

the translations and rotations are easily identified as the zero-frequency modes. The electronic coordinates are defined as positions of electrons relative to the nuclear center of mass with a fixed orientation, i.e. in the Eckart frame [43]. The Coriolis coupling (between nuclear vibrations and rotations) is excluded. While the removal of molecular rotations is an approximation [43], it is an appropriate one for ultrafast (fs-ps) chemical dynamics simulations, and we provide further justification in the Discussion.

The full molecular vibronic Hamiltonian is given by

$$\hat{H}_{\text{mol}} = - \sum_i^{N_e} \frac{\nabla_i^2}{2} + \sum_i^{N_e} v_{\text{en}}(\mathbf{r}_i, \mathbf{Q}) + \sum_{i < j}^{N_e} v_{\text{ee}}(\mathbf{r}_i, \mathbf{r}_j) + \sum_{\nu}^{N_{\text{mode}}} \frac{P_{\nu}^2}{2} + V_{\text{nn}}(\mathbf{Q}), \quad (1)$$

where \mathbf{r}_i is the position of the electron i in the Eckart frame, Q_{ν} is the normal mode coordinate for mode ν , $P_{\nu} = -i\partial/\partial Q_{\nu}$ is the corresponding momentum, N_{mode} is the number of vibrational modes, N_e is the number of electrons, and v_{en} , v_{ee} , and V_{nn} are electron-nuclear, electron-electron, and nuclear-nuclear interaction potentials, respectively. We use atomic units ($\hbar = m_e = e = 4\pi\epsilon_0 = 1$) here and throughout this paper.

To reduce the electronic basis size, we adopt a basis of orthonormal spin orbitals that depend parametrically on the nuclear positions, $\phi_p(\mathbf{x}; \mathbf{Q}) = \varphi_p(\mathbf{r}; \mathbf{Q})\sigma_p(s)$, where \mathbf{x} is a vector of electronic spatial coordinates \mathbf{r} and a spin coordinate s , i.e. $\mathbf{x} = \{\mathbf{r}, s\}$, and φ_p and σ_p are spatial and spin functions of the spin orbital, respectively.

We express the molecular vibronic wavefunction using Slater determinants of the position-dependent spin orbitals for electronic degrees of freedom and Hartree products of harmonic oscillator eigenstates of normal modes for vibrational degrees of freedom. In the second quantization representation, the Slater determinants and the Hartree product can be expressed as occupation number vectors (ONVs). An electronic ONV for a Slater determinant is written as $|\mathbf{n}\rangle_{\text{e}} = |n_1 \cdots n_{N_{\text{o}}}\rangle_{\text{e}}$, where n_j is the occupation of the j -th spin orbital and N_{o} is the number of spin orbitals, while a vibrational ONV for a Hartree product is given as $|\mathbf{v}\rangle_{\text{n}} = |v_1 \cdots v_{N_{\text{mode}}}\rangle_{\text{n}}$, where v_{ν} is the occupation (Fock state) of mode ν . Therefore, our wavefunction ansatz becomes

$$|\Psi(t)\rangle = \sum_{\mathbf{v}} \sum_{\mathbf{n}} C_{\mathbf{v}\mathbf{n}}(t) |\mathbf{v}\rangle_{\text{n}} \otimes |\mathbf{n}\rangle_{\text{e}}, \quad (2)$$

where $C_{\mathbf{v}\mathbf{n}}(t)$ is the coefficient for the collective occupation $\mathbf{v} \cup \mathbf{n}$.

Sasmal and Vendrell [24] showed that above ansatz transforms the molecular vibronic Hamiltonian to the

second quantization representation [24]:

$$\begin{aligned} \hat{H}_{\text{mol}} = & \sum_{pq}^{N_o} h_{pq}(\hat{\mathbf{Q}}) \hat{a}_p^\dagger \hat{a}_q + \frac{1}{2} \sum_{pqrs}^{N_o} v_{pqrs}(\hat{\mathbf{Q}}) \hat{a}_p^\dagger \hat{a}_q^\dagger \hat{a}_s \hat{a}_r \\ & + \sum_{pq}^{N_o} \sum_{\nu}^{N_{\text{mode}}} \left(id_{\nu,pq}(\hat{\mathbf{Q}}) \cdot \hat{P}_\nu - g_{\nu,pq}(\hat{\mathbf{Q}}) \right) \hat{a}_p^\dagger \hat{a}_q \quad (3) \\ & + \sum_{\nu}^{N_{\text{mode}}} \frac{\hat{P}_\nu^2}{2} + V_{\text{nn}}(\hat{\mathbf{Q}}), \end{aligned}$$

where h_{pq} , $d_{\nu,pq}$, $g_{\nu,pq}$, and v_{pqrs} are electron integrals whose definitions are given in the Supplemental Material. The \mathbf{Q} -dependence of spin-orbitals and Slater determinants are absorbed into the electronic integrals, and the couplings between nuclear and electronic degrees of freedom appear as products of the electron integrals and fermionic ladder operators in the Hamiltonian. The terms akin to nonadiabatic coupling terms in electronic structure ($d_{\nu,pq}$ and $g_{\nu,pq}$) are introduced because the nuclear kinetic energy operator acts on the spin orbital basis functions [24]. The mass-weighted normal mode position $\hat{Q}_\nu = \sqrt{1/2\omega_\nu}(\hat{b}_\nu^\dagger + \hat{b}_\nu)$ and the conjugate momentum $\hat{P}_\nu = i\sqrt{\omega_\nu/2}(\hat{b}_\nu^\dagger - \hat{b}_\nu)$ operators for mode ν can be expressed in terms of the bosonic ladder operators $\{\hat{b}_\nu\}$ and $\{\hat{b}_\nu^\dagger\}$ where ω_ν is the (approximate) harmonic frequency of the normal mode ν . Therefore, the terms depending on the normal mode coordinates in Eq. 3 can be expressed in terms of the bosonic ladder operators by using a Taylor series expansion about a reference geometry \mathbf{Q}_0 up to a reasonable order.

For fixed Taylor expansion orders, ω_ν and \mathbf{Q}_0 only affect the accuracy of our approach by the number of harmonic eigenstates required to describe the wavefunction. In other words, a quantum simulator with lower oscillator noise can tolerate lower-accuracy parameters, including approximations derived from the electronic integral Taylor expansions. For practical cases in the near term, we expect that density functional theory (DFT) will provide an ideal balance between accuracy and classical computational cost when finding \mathbf{Q}_0 and ω_ν , and Kohn-Sham orbitals provide a compact spin orbital basis [44].

In general, the orbital vibronic coupling functions $d_{\nu,pq}$ and $g_{\nu,pq}$ can be extremely localized and non-analytical at some nuclear geometries. This requires a high-order expansion in terms of the bosonic ladder operators in Eq. 3, which greatly increases the number of terms in the Hamiltonian. One way to reduce the expansion order would be a unitary transformation of orbitals for which the derivative couplings vanish, which must satisfy $\partial \mathbf{c} / \partial Q_\nu + \mathbf{d}_\nu \mathbf{c} = 0$, where \mathbf{c} is the transformation matrix to the resulting set of “diabatic” orbitals, $\eta_m = \sum_l c_{lm} \psi_l$. This transformation is identical in form to the many-body BO state diabaticization condition [14]. A set of strictly diabatic states does not exist in general for multi-electron states in multi-mode systems [45], and the same arguments apply for orbitals. However, because our goal

is simply to achieve a low-order expansion in terms of \mathbf{Q} , we can use “quasi-diabatic” orbitals where the above strict diabaticization condition is not satisfied. These orbitals can likewise borrow techniques from BO state diabaticization [46].

A. Analog quantum simulation

We now introduce our approach to map the Hamiltonian \hat{H}_{mol} onto an analog quantum device to perform a pre-BO simulation. Such a mapping must satisfy the symmetry requirements of fermions (electrons) and bosons (vibrations), given by their (anti-)commutation relations. Ideally, we would like to map both types of degrees of freedom onto a device with native fermionic and bosonic degrees of freedom. There are quantum architectures that contain bosonic modes such as ion traps and circuit quantum electrodynamics (cQED) devices, and some basic architectures with controllable fermionic states [47, 48] have been proposed. However, there is currently no practical quantum architecture that contains both degrees of freedom with individual control. Instead, we will use a fermion-qubit mapping to represent spin orbital ladder operators with non-local qubit operators [49, 50]. This allows us to use ion traps or cQED, since both have qubit levels in addition to their bosonic modes. We will refer to architectures that contain multiple qubits and bosonic modes with controllable coupling between them as “coupled multi-qubit-boson” (cMQB) devices, which are a subset of mixed qudit-boson (MQB) devices [39].

An illustration of our pre-BO analog simulation method in comparison with the BO framework is summarized in Fig. 1. After finding a nuclear position dependent spin orbital basis (Fig. 1a) and its expansion coefficients in Eq. 3, the pre-BO wavefunction (Fig. 1b) is encoded on the cMQB simulator, e.g. on a trapped-ion device with ion electronic states representing electronic ONVs, and ion motional modes representing the nuclear component of the wavefunction (Fig. 1c). In contrast, existing classical/quantum algorithms in the BO framework require the pre-calculation of BO electronic states (Fig. 1d) with the spin orbital basis. The vibronic wavefunction is then propagated on a truncated BO basis (Fig. 1e), which can result in inaccurate dynamics simulations.

1. Fermion-qubit mapping

For the electronic degrees of freedom, we use the Jordan-Wigner transformation which directly maps the occupation number of a spin orbital to the qubit state [49]. However, other fermion-qubit mappings could be equivalently employed. The fermionic creation operator for spin orbital p is mapped to a tensor product of Pauli operators $(\hat{X}_k, \hat{Y}_k, \hat{Z}_k)$ for qubits by $\hat{a}_p = \hat{Z}_1 \otimes \cdots \otimes \hat{Z}_{p-1} \otimes (\hat{X}_p + i\hat{Y}_p)$, and the annihilation opera-

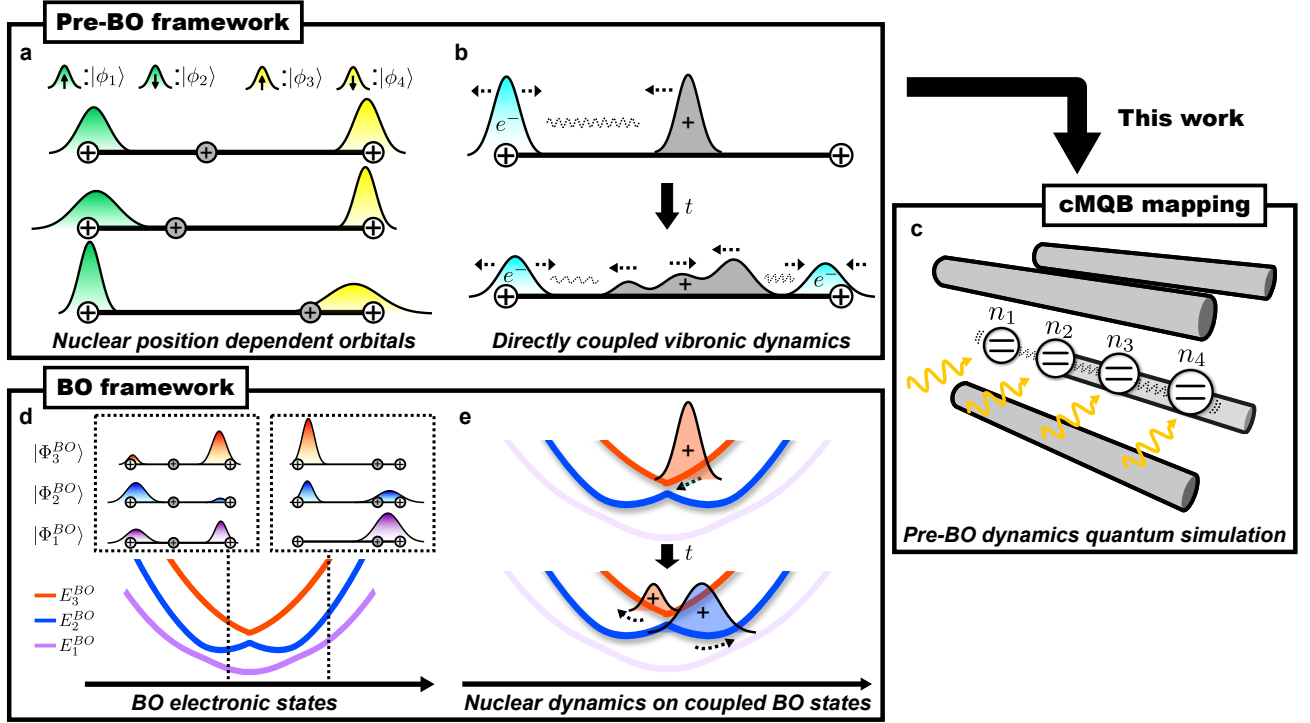


FIG. 1. Illustration of analog quantum simulation approaches for molecular vibronic dynamics using trapped-ion architectures. **a**, The electronic wavefunction is given in terms of spin orbitals. Each diabatic spatial orbital, which depends on the nuclear positions, yields two spin orbitals with opposite spins: $|\phi_1\rangle$ and $|\phi_2\rangle$ (green), and $|\phi_3\rangle$ and $|\phi_4\rangle$ (yellow). Only the motion of a single ion (grey) is shown. **b**, Molecular vibronic dynamics are simulated based on the pre-BO representation with interactions among electronic (cyan) and nuclear (grey) degrees of freedom. **c**, In this work, we propose a coupled multi-qubit boson (cMQB) approach which maps occupation numbers $\{n_p\}$ of spin orbitals $\{|\phi_p\rangle\}$ to qubits and nuclear motions to bosonic modes coupled to the qubits, and thus can perform pre-BO dynamics quantum simulations with a complete electronic basis within a given orbital basis set. **d**, Existing quantum/classical algorithms rely on BO states $\{|\Phi_i\rangle\}$ with potential energy surfaces $\{E_i\}$ found by solving the electronic time-independent Schrödinger equation using the orbital basis at fixed nuclear positions prior to the simulation. **e**, Molecular vibronic dynamics are solved in the BO framework by propagating the nuclear wavefunction (red and blue densities) on a truncated set of coupled BO states. The truncation leads to a deviation from exact results shown in **b**.

tor is its Hermitian conjugate. The general expression for the cMQB Hamiltonian becomes a sum of tensor products of multiple bosonic and qubit operators, i.e.

$$\hat{H}_{\text{cMQB}} = \sum_I \hat{H}_I = \sum_I f_I \left(\{\hat{b}_\nu\}, \{\hat{b}_\nu^\dagger\} \right) \bigotimes_{k=1}^{N_q} \hat{P}_k^I, \quad (4)$$

where N_q is the number of qubits, \hat{P}_k^I is one of the identity or Pauli operators for the k -th qubit ($\hat{P}_k \in \{\hat{I}_k, \hat{X}_k, \hat{Y}_k, \hat{Z}_k\}$) in the I -th Pauli string, and f_I is a function of bosonic ladder operators \hat{b}_ν and \hat{b}_ν^\dagger coupled to the I -th Pauli string. Although the fermion-qubit mapping and the corresponding electronic basis is not spin-adapted, the Hamiltonian commutes with total electronic spin z -projection and square (\hat{S}_z and \hat{S}^2) operators. Correspondingly, the electronic part of the molecular vibronic state $|\mathbf{n}\rangle_e$ in our ansatz (Eq. 2) is mapped to the multi-qubit state $|\mathbf{q}\rangle_q = |q_1 \cdots q_{N_q}\rangle_q$ of the cMQB device, while the multi-mode vibrational wavefunction is directly mapped to the bosonic degrees of freedom (Fig. 1c). A schematic illustration of a circuit for pre-BO

dynamics simulation with the cMQB mapping consists of initialization, time-evolution, and measurement is shown in Fig. 2.

2. Initialization

As with any quantum dynamics simulation, our approach requires a robust preparation of the initial state which can be generated by a unitary operator \hat{F} (Fig. 2a). For most applications in photochemical dynamics we can assume that the initial state is well represented as a product state of electronic and nuclear components of the wavefunction which can be prepared by $\hat{F} = \hat{F}_e \otimes \hat{F}_n$, with separate operations on qubits with \hat{F}_e and motional states with \hat{F}_n . According to the Franck-Condon approximation, the equilibrium nuclear state is unperturbed by photoexcitation and the excitation is instantaneous. This means the initial state can be prepared with a ground (or coherent) nuclear state, and with qubit states corresponding to the photoexcited spin orbital occupation.

Future devices with longer coherence times and more sophisticated quantum control will allow for increasingly accurate initial state preparation. For example, controlled dissipation of the simulator could be used to prepare the vibronic ground state wavefunction, with the fidelity approaching 1 for longer experimental times. The dynamics could then be initialized by a purely electronic (Franck-Condon) or vibronic transition dipole operator. By implementing a time-dependent Hamiltonian with the transition dipole operator, our approach can also serve as a platform for the explicit simulation of vibronic effects in light-matter interactions.

3. Coupled multi-qubit-boson time-evolution operator

The direct implementation of the approach outlined above requires the simultaneous control of all degrees of freedom in the simulation. This becomes impractical for large molecules with many vibrational modes. Therefore, instead of simultaneous evolution, we can use Trotterization [51] of the time-evolution operator. Trotterization approximates the time-evolution operator as a product of operators, each of which corresponds to a term \hat{H}_I in Eq. 4. The Trotter time-evolution operator is given by $\hat{U}_{\text{cMQB}}(t) \approx \left(\prod_I^{N_{\text{op}}} \hat{U}_I(t/N_t) \right)^{N_t} \equiv \hat{U}(\Delta t)^{N_t}$, where N_{op} is the number of divided operators and N_t is the number of the Trotter steps (Fig. 2b).

The time-evolution operator for each term in our Hamiltonian (Eq. 4) is given by

$$\begin{aligned} \hat{U}_I(t) &= \exp(-it\hat{H}_I) \\ &= \exp\left(-itf_I\left(\{\hat{b}_\nu\}, \{\hat{b}_\nu^\dagger\}\right) \bigotimes_{k=1}^{N_q} \hat{P}_k^I\right) \\ &= \hat{\Lambda}^I \exp\left(-itf_I\left(\{\hat{b}_\nu\}, \{\hat{b}_\nu^\dagger\}\right) \otimes \hat{X}_{q_0}^I\right) \hat{\Lambda}^{I\dagger}. \end{aligned} \quad (5)$$

where $\hat{\Lambda}^I$ is a product of tensor products of Clifford gates (Hadamard, phase, and CNOT gates) to propagate the coupling between bosonic mode(s) and a single qubit q_0^I generated by a laser-ion interaction to multiple qubits for the desired Pauli strings for \hat{H}_I . In Fig. 2b, we show an example cMQB time-evolution operator $\hat{U}_I(\Delta t) = \exp(-i\theta\Delta t(\hat{b}_1 + \hat{b}_1^\dagger)\hat{Y}_2\hat{Z}_3\hat{Y}_4)$, which can be achieved by a sequence of digital and analog quantum operations: $\hat{S}_4\hat{S}_2\hat{H}_3\hat{C}_{34}\hat{C}_{32}\exp(-i\theta\Delta t(\hat{b}_1 + \hat{b}_1^\dagger)\hat{X}_3)\hat{C}_{32}\hat{C}_{34}\hat{H}_3\hat{S}_2^\dagger\hat{S}_4^\dagger$ where \hat{C}_{ij} is the CNOT gate for the control qubit i and the target qubit j , and \hat{H}_i and \hat{S}_i are the Hadamard and phase gates for qubit i , respectively. Therefore, this approach can be considered a digital-analog quantum simulation [52] because the gates involved in generating qubit entanglement take a digital form. A fully analog form of the time-evolution could be achieved using time- and spin-dependent squeezing/displacement operators on the collective ionic mo-

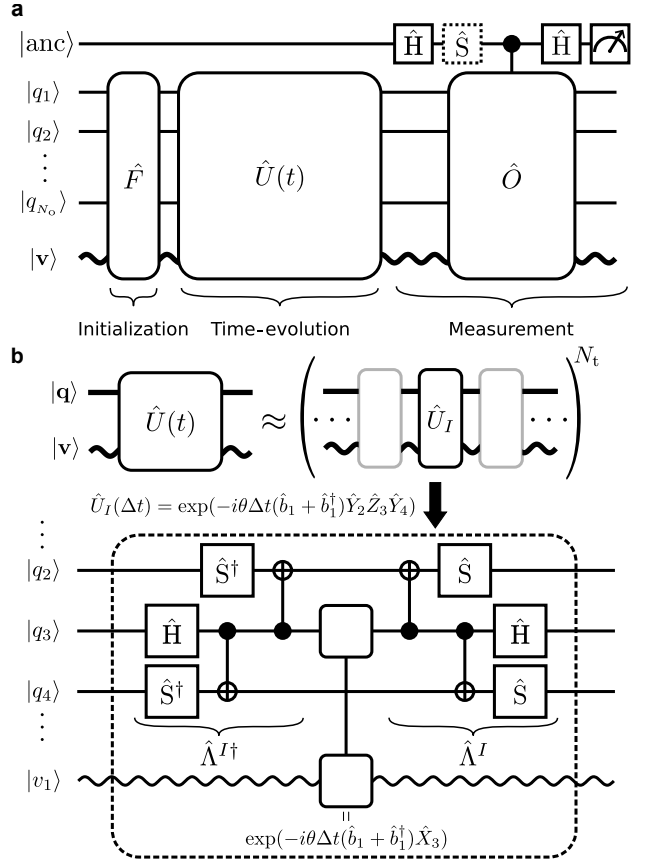


FIG. 2. A schematic quantum circuit diagram for pre-BO vibronic dynamics simulation with the cMQB approach. Straight lines represent qubits and wavy lines represent the motional modes. **a**, A simulation consists of initialization, time-evolution, and measurement stages. An initial vibronic state can be prepared by a unitary operator \hat{F} . The initial state then propagated by the time-evolution operator $\hat{U}(t)$. Finally, an expectation value can be measured with Hadamard tests with the corresponding operator \hat{O} controlled by an ancilla qubit state (represented by a black circle) using Hadamard (\hat{H}) and phase gates (\hat{S}). Real and imaginary parts of the expectation value are obtained with and without the phase gate, respectively. **b**, Trotterization of the time-evolution operator $\hat{U}(t)$ and the digital-analog circuit for an example Trotterized cMQB operator $\hat{U}(\Delta t) = \exp(-i\theta\Delta t(\hat{b}_1 + \hat{b}_1^\dagger)\hat{Y}_2\hat{Z}_3\hat{Y}_4)$. CNOT gates are represented by symbols with a black circle for the control qubit, connected to an open circle for the target qubit.

tions [53]; however, for the remainder of this paper we consider the digital-analog approach.

cMQB devices such as trapped ions and cQED typically use bosonic modes to achieve entangling gates in digital quantum algorithms. The quantum gates necessary to implement $\hat{\Lambda}^I$ are thus readily achieved with these architectures. However, because the entangling gates require a bosonic mode, certain bosonic modes must be reserved from those used to simulate nuclear vibrational degrees of freedom. The total number of bosonic modes

in the simulator must therefore be at least one greater than the total number of molecular vibrational modes.

4. Measurement

Our approach encodes the electronic degrees of freedom of the vibronic wavefunction as an ONV, and nuclear degrees of freedom are mapped to the bosonic modes. This difference in encoding means that all nuclear observables can be measured directly from the simulator, whereas some electronic and vibronic observables will depend on the electronic orbital basis functions. In general, the expectation values of observables can be obtained with Hadamard tests [54] for the corresponding unitary operator \hat{O} , in which an ancilla qubit in a superposition of $|0\rangle$ and $|1\rangle$ states is used to control the operator on the wavefunction (Fig. 2a). Measurement of the ancilla in the \hat{X} basis yields the real component of the expectation value of the operator, and the \hat{Y} basis measurement gives the imaginary component.

For example, a one-electron property $\langle \hat{O}_{1e} \rangle \equiv \langle \Psi | \hat{O}_{1e} | \Psi \rangle$ is obtained by the sum of the measured elements of the one-electron reduced density matrix (1RDM), $\langle \hat{a}_p^\dagger \hat{a}_q \rangle$, weighted by the integrals $\langle \phi_p | \hat{O}_{1e} | \phi_q \rangle$ for spin orbitals p and q . The 1RDM is calculated from the quantum simulator by measuring expectation values of Pauli strings, whereas the integrals are obtained on a classical computer. Conversely, the expectation value of a unitary nuclear operator that can be expressed as an exponential, $\hat{O}_n = \exp(\hat{A}_n)$, can be implemented directly on the analog simulator with an effective Hamiltonian $\hat{H}_n^{\text{eff}} = i\hat{A}_n/\tau$ by evolving for a time τ .

Real-space density functions are important observables for characterizing the dynamics of a molecule. They are expressed in terms of the real-space projection operator, $|\underline{\mathbf{x}}, \mathbf{Q}\rangle\langle \underline{\mathbf{x}}, \mathbf{Q}|$ where $\underline{\mathbf{x}} = \{\mathbf{x}_1, \dots, \mathbf{x}_{N_e}\}$. For example, the projection operator for the joint nuclear normal modes and electronic density is $N_e \int d\underline{\mathbf{x}} \delta(\mathbf{r} - \mathbf{r}_1) |\underline{\mathbf{x}}, \mathbf{Q}\rangle\langle \underline{\mathbf{x}}, \mathbf{Q}|$, which yields

$$\rho(\mathbf{r}, \mathbf{Q}, t) = \sum_{p,q} \left[\varphi_p^*(\mathbf{r}; \mathbf{Q}) \varphi_q(\mathbf{r}; \mathbf{Q}) \delta_{\sigma_p \sigma_q} \right. \\ \left. \times \mathcal{F}_{\mathbf{k}} \left\{ \left\langle \hat{a}_p^\dagger \hat{a}_q \bigotimes_{\nu}^{\text{Nmode}} \hat{D}_\nu(i\xi_\nu) \right\rangle \right\}(\mathbf{Q}) \right], \quad (6)$$

where $\xi_\nu = k_\nu/\sqrt{2\omega_\nu}$ is a frequency weighted momentum coordinate for mode ν . The variable $\mathbf{k} = \{k_1, \dots, k_{N_{\text{mode}}}\}$ is the momentum space variable associated with the normal mode \mathbf{Q} , and $\mathcal{F}_{\mathbf{k}}\{f(\mathbf{k})\}(\mathbf{Q})$ represents a multi-dimensional Fourier transform of the function $f(\mathbf{k})$ to nuclear normal mode coordinate (\mathbf{Q}) space. Eq. 6 exploits the tomography of the nuclear characteristic function using displacement operators \hat{D}_ν [55], where the Fourier transform is performed numerically on the expectation values measured on grid points for displace-

ment operators with different values of ξ_ν . The displacement operator in Eq. 6 can be implemented on a cMQB device, and the range and resolution of the density is controlled by the separation of grid points ξ_ν .

Electron and nuclear densities can be obtained by integrating out other degrees of freedom, given by $\rho_e(\mathbf{r}) = \int d\mathbf{Q} \rho(\mathbf{r}, \mathbf{Q}, t)$ and $\rho_n(\mathbf{Q}) = \int d\mathbf{r} \rho(\mathbf{r}, \mathbf{Q}, t)$, respectively. Measurement of the nuclear density, which provides the basis for the analysis of chemical reactions such as isomerization and bond dissociation, simplifies to

$$\rho_n(\mathbf{Q}, t) = \mathcal{F}_{\mathbf{k}} \left\{ \left\langle \bigotimes_{\nu}^{\text{Nmode}} \hat{D}_\nu(i\xi_\nu) \right\rangle \right\}(\mathbf{Q}), \quad (7)$$

due to the orthonormality of spin orbitals at all \mathbf{Q} . Reduced vibrational densities are likewise found by only measuring the characteristic functions of the desired vibrational modes.

B. Connection to the Born-Oppenheimer framework

If we define the electronic Hamiltonian $\hat{H}^e(\mathbf{Q})$ as the first two terms of Eq. 3 at a fixed nuclear position \mathbf{Q} , then we can find an electronic Hamiltonian matrix $\mathbf{H}^e(\mathbf{Q})$ with elements $H_{\mathbf{m}\mathbf{n}}^e(\mathbf{Q}) = \langle \mathbf{m} | \hat{H}^e(\mathbf{Q}) | \mathbf{n} \rangle_e$, where only electronic degrees of freedom are integrated. The Hamiltonian matrix can be transformed by a unitary matrix $\mathbf{W}(\mathbf{Q})$ to give $\mathbf{E}^e(\mathbf{Q}) = \mathbf{W}(\mathbf{Q})\mathbf{H}^e(\mathbf{Q})\mathbf{W}^\dagger(\mathbf{Q})$. When $\mathbf{E}^e(\mathbf{Q})$ is a fully diagonal matrix, we arrive at the exact (full configuration interaction, FCI) solution to the electronic structure problem. In practice, full diagonalization is intractable on classical computers, so the eigenvalues of a submatrix of $\mathbf{H}^e(\mathbf{Q})$ may be found instead. Iterative diagonalization is typically used to further reduce the cost, and the number of eigenvalues found, N_{BO} , can be less than the rank of the (sub)matrix. The BO electronic states are the corresponding eigenfunctions (Fig. 1d), and molecular dynamics can be expressed by the Born-Huang expansion as nuclear dynamics on multiple BO states:

$$\Psi_{\text{BH}}(\underline{\mathbf{x}}, \mathbf{Q}, t) \\ = \sum_j^{N_{\text{BO}}} \chi_j^{\text{BO}}(\mathbf{Q}, t) \Phi_j^{\text{BO}}(\underline{\mathbf{x}}; \mathbf{Q}) \\ = \sum_j^{N_{\text{BO}}} \sum_{\mathbf{v}} T_{j\mathbf{v}}(t) \mathbf{v}(\mathbf{Q}) \sum_{\mathbf{n}} W_{j\mathbf{n}}(\mathbf{Q}) \mathbf{n}(\underline{\mathbf{x}}; \mathbf{Q}), \quad (8)$$

where $\mathbf{n}(\underline{\mathbf{x}}; \mathbf{Q}) = \langle \underline{\mathbf{x}}, \mathbf{Q} | \mathbf{n} \rangle$ and $\mathbf{v}(\mathbf{Q}) = \langle \mathbf{Q} | \mathbf{v} \rangle$ are the real space wavefunctions of the electronic and nuclear ONVs, i.e. the Slater determinant and Hartree product of single particle basis functions, respectively. $W_{j\mathbf{n}}$ is an element of \mathbf{W} , $\Phi_j^{\text{BO}}(\underline{\mathbf{x}}; \mathbf{Q}) = \sum_{\mathbf{n}} W_{j\mathbf{n}} \mathbf{n}(\underline{\mathbf{x}}; \mathbf{Q})$ is the j -th BO state, and $\chi_j^{\text{BO}}(\mathbf{Q}, t) = \sum_{\mathbf{v}} T_{j\mathbf{v}}(t) \mathbf{v}(\mathbf{Q})$ is the corresponding time-dependent BO-projected nuclear wavefunction with an expansion coefficient $T_{j\mathbf{v}}(t)$ (Fig. 1e).

Without spin-orbit coupling, the electronic Hamiltonian commutes with the electron number operator, and the z -component and square of the total electron spin angular momentum operator. The maximum number of BO electronic states is thus equal to the number of configuration state functions (CSFs, i.e. spin-adapted linear combinations of Slater determinants) with a fixed electron count and spin, N_{CSF} , which we will discuss in more detail in Sec IV. The summation over the BO states in Eq. 8 is exact within the given orbital basis set only when $N_{\text{BO}} = N_{\text{CSF}}$. The relation between the Born-Huang expansion and our ansatz (Eq. 2) becomes clear via the relation $\sum_j^{N_{\text{CSF}}} \sum_{\mathbf{v}'} T_{j\mathbf{v}'}(t) (W_{j\mathbf{n}})_{\mathbf{v}\mathbf{v}'} = C_{\mathbf{v}\mathbf{n}}(t)$, where $(W_{j\mathbf{n}})_{\mathbf{v}\mathbf{v}'} = \int d\mathbf{Q} \mathbf{v}^*(\mathbf{Q}) W_{j\mathbf{n}}(\mathbf{Q}) \mathbf{v}'(\mathbf{Q})$. However, N_{CSF} scales rapidly with the orbital basis set size whereas N_{BO} must be kept small for practical simulations. Therefore, the GBOA is employed ($N_{\text{BO}} < N_{\text{CSF}}$) to reduce the computational cost of the BO state calculations and time-propagation of the molecular vibronic state (Fig. 1e). In contrast, our ansatz (Eq. 2) is exact within the given vibronic basis by definition (Fig. 1c).

III. NUMERICAL TEST

In this section, we show a proof-of-principle demonstration of our analog simulation approach using the one-dimensional, two-electron Shin-Metiu model [56, 57] and its implementation on a trapped ion quantum computer. The model consists of two electrons, two fixed ions, and one moving ion between the fixed ions displaced by a distance $L = 5.4$ a.u. (Fig. 3a), where the origin is set to the middle point of the two fixed ions. The computational details for all simulations performed in this section, including the parameters for the model Hamiltonian, are given in the Supplemental Material and Refs. 14, 56–58.

We construct the electronic Fock space with four spin orbitals $\{|\phi_i\rangle\}$ using the spin-up and spin-down configurations of two diabatic spatial orbitals, η_a and η_b in Fig. 3c and 2d, respectively, i.e. $\varphi_1 = \varphi_2 = \eta_a$, and $\varphi_3 = \varphi_4 = \eta_b$. As a result, a total of four ions ($\max(N_{\text{mode}} = 1, N_{\text{o}} = 4)$) are needed in the experimental trapped ion setup for the simulation. The diabatic orbitals were obtained by numerically integrating two adiabatic orbitals from the one-electron Shin-Metiu Hamiltonian [56] subject to the diabaticization condition. The resulting orbitals are localized around the left and right fixed ions, but delocalize slightly as the moving ion approaches the fixed ion (Fig. 3c and 3d). We replaced the Coulomb potential for V_{nn} with a harmonic potential to simplify the Hamiltonian and to confine the spatial extent of the wavefunction. The one- and two-electron integrals are truncated at first order in the nuclear position: $v(\hat{Q}) \approx v_0 + v_1 \hat{Q}$, where $\hat{Q} = (\hat{b}^\dagger + \hat{b})/\sqrt{2\omega}$ with ladder operators \hat{b}^\dagger and \hat{b} of our single mode with frequency ω of the harmonic nuclear repulsion potential. With these approximations, the mapped Hamiltonian can be written

as

$$\hat{H}_{\text{cMQB}} = \omega \hat{b}^\dagger \hat{b} + \sum_I (V_0^I + V_1^I (\hat{b}^\dagger + \hat{b})) \hat{P}_1^I \hat{P}_2^I \hat{P}_3^I \hat{P}_4^I. \quad (9)$$

The model system has only a single nuclear degree of freedom, meaning the normal mode coordinate is equal to the position of the moving ion multiplied by the square root of the mass of the ion M , i.e. $Q = \sqrt{M}R$. We show results in terms of the unweighted coordinate R rather than Q to show the ion and electrons in the same position space.

We initialized the molecular state as $|\Psi(0)\rangle = \hat{D}(R_0 \sqrt{M\omega/2})|0\rangle_{\text{n}} \otimes |1100\rangle_{\text{q}}$ (Fig. 3d), where the ground state wavefunction of the harmonic oscillator for bosonic degrees of freedom is displaced by $R_0 = 0.1$ a.u. in real space, and electrons are in the closed shell configuration of the orbital η_a (Fig. 3b). To achieve the initial state experimentally on an ion trap, we would first prepare the ground state of two bosonic modes and of each of the qubits, $|0000\rangle_{\text{q}}$. The additional bosonic mode is required to implement qubit entanglement operations. Then, we would apply a digital quantum operation $\hat{X}_1 \hat{X}_2$, and subsequently apply the displacement operator using spin-dependent force on ions with a laser interaction [59].

For the time-evolution, we assume that the base Hamiltonian of the ion trap (the first term in Eq. 9) is always present during the simulation and rescale the Trotter steps to compensate for it [39]. The Trotterized cMQB time-evolution operators could be achieved by either one of methods introduced in Sec. II A 2. To achieve the first approach, we would apply a series of digital quantum gates on the trapped ions with single-ion addressing. The second bosonic mode would be used to apply the entangling gates [59].

In Fig. 3, we show the density functions $\rho(\mathbf{r}, \mathbf{Q}, t)$ obtained from exact time-evolution, Trotterized cMQB time-evolution, and the GBOA. Experimentally, determination of the density function would require an ancilla qubit which controls the operator for the density measurement. Controlled Pauli strings correspond to CNOT and single-qubit gates, and controlled displacement operators can be achieved with a spin-dependent force on the trapped ions [55, 59]. The sum of all orbital pairs with Fourier transforms over a grid of displacements yields the density, as shown in Eq. 6. For this example, only 12 sets of measurements are required: two Pauli strings with four on-diagonal and two non-zero off-diagonal pairs. This number of measurements can be halved because the densities of the two spin components are equal. We can obtain a nuclear density resolution of 0.02 a.u. using a grid spacing of 1.26 a.u. in the momentum space with 250 points.

The Trotterized cMQB time-evolution reproduces the exact density with converged Trotter step $\Delta t = 5.6$ a.u (Fig. 3f,i), where the fidelity of the corresponding wavefunction is reported in the Supplemental Material. At $t = 1514.4$ a.u., the non-zero densities on both sides of the fixed ions (Fig. 3h,i) indicates that the moving ion

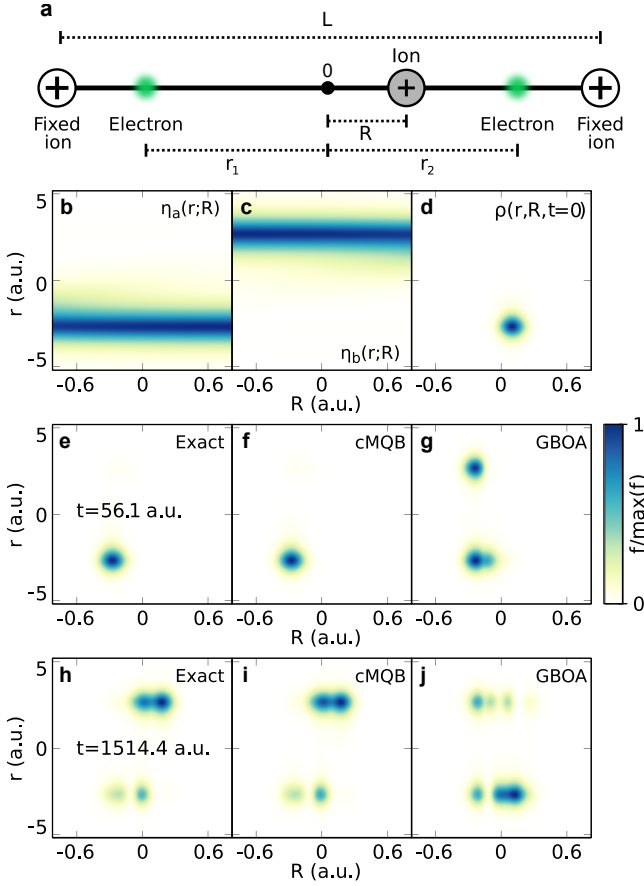


FIG. 3. Results for theoretical simulations of the one-dimensional, two-electron Shin-Metiu model with exact time-evolution, cMQB time-evolution, and the GBOA. **a**, The model system consists of two fixed ions (white circles) displaced by distance L , a moving ion (grey circle) at a position R , and two electrons (green circles) at positions r_1 and r_2 . The origin is the average of the fixed ion positions. The diabatic orbitals: **b**, $\eta_a(r;R)$ localized around the left fixed ion, and **c**, $\eta_b(r;R)$ localized around the right fixed ion. The density functions $\rho(r,R,t)$ at $t = 56.1$ a.u. (**e–g**) and $t = 1514.4$ a.u. (**e–g**), with exact time-evolution (**e** and **h**), cMQB time-evolution ($\Delta t = 5.6$ a.u.) (**f** and **i**), and GBOA (**g** and **j**). Spatial functions in **b–j** are normalized to their maximum values.

induces electron transfer from the left to the right fixed ions via vibronic coupling.

To highlight inaccuracies that originate from the GBOA, we perform equivalent dynamics simulations in the BO framework (Eq. 8) with a truncated BO basis. In this simulation, we prepare the same initial state as the pre-BO simulation (Fig. 3d). For two electrons in two spatial orbitals with a singlet spin multiplicity, $N_{\text{CSF}} = 3$. The ground BO state is excluded from the dynamics for the GBOA ($N_{\text{BO}} = 2$), which has relatively small NACs with the first excited state.

The density functions obtained with the GBOA are shown in Figs. 3g,j. Within a short simulation time (56.1 a.u.), there is a spurious electron transfer from the left

fixed ion to the right (Fig. 3g). This electron transfer does not occur in the exact limit (Fig. 3e) and the Trotterized cMQB time-evolution (Fig. 3f) due to vibronic coupling to the ground BO state. As a result, the subsequent density deviates even further, as seen in Fig. 3j. This demonstrates how the GBOA may result in inaccurate molecular vibronic dynamics when a molecule reaches an unanticipated NAC region coupled to a BO state outside of the truncated BO basis. Our method spans the FCI space without basis set truncation with a given orbital basis set, so there is no need to pre-determine the truncation of electronic states.

IV. DISCUSSION

We first compare the resource and computational costs of our cMQB pre-BO analog simulation approach with those of existing classical and quantum algorithms, where the advantages of our approach are highlighted in Fig. 4.

The number of qubits required for our approach is equal to the number of spin orbitals, N_o . On the other hand, the equivalent number of electronic states in the BO framework corresponds to the exact Born-Huang expansion limit ($N_{\text{BO}} = N_{\text{CSF}}$). Therefore, the classical resources scale proportionally to N_{CSF} for a fixed spin-multiplicity, which can be calculated according to the Weyl’s formula for the corresponding total spin angular momentum S :

$$N_{\text{CSF}}(S, N_o, N_e) = \frac{2S+1}{N_o/2+1} \binom{N_o/2+1}{N_e/2-S} \binom{N_o/2+1}{N_e/2+S+1}. \quad (10)$$

Here, we discuss singlet states ($S = 0$) since most ground-state electron configurations of neutral organic molecules are singlets since they have an even number of electrons and a lack of orbital degeneracy. The number of singlet CSFs is minimum ($O(N_o^2)$) when $N_e = 2$ or $N_e = N_o - 2$, and maximum ($O(2^{N_o}/N_o^2)$) when $2N_e = N_o$ for a fixed N_o . Practical simulations fall in between these two ranges with a number of orbitals roughly proportional to the number of electrons, with the ratio depending on the basis set. For example, conjugated polyene chains with a double-zeta basis set have $N_o/N_e = 6$. In general, the classical resources scale as $O(N_o^{-2}(m(m-1)^{1/m-1})^{N_o})$ for $N_o = mN_e$ ($m > 1$) at large N_o limit. In Fig. 4a, we show classical resource scaling for singlet states in comparison with our approach. The linear scaling of our approach has a clear advantage over classical methods, even over the minimum N_{CSF} case for $N_o > 6$.

For the nuclear degrees of freedom, the classical simulation has an exponential resource scaling of $O(\prod_{\nu=1}^{N_{\text{mode}}} N_{\nu,\text{bas}})$ where $N_{\nu,\text{bas}}$ is the size of basis for mode ν . Our encoding on cMQB simulators has a linear scaling $O(N_{\text{mode}})$, which is equal to that of an MQB mapping [39].

Like classical methods, the number of qubits can be reduced by using a complete active space. The active

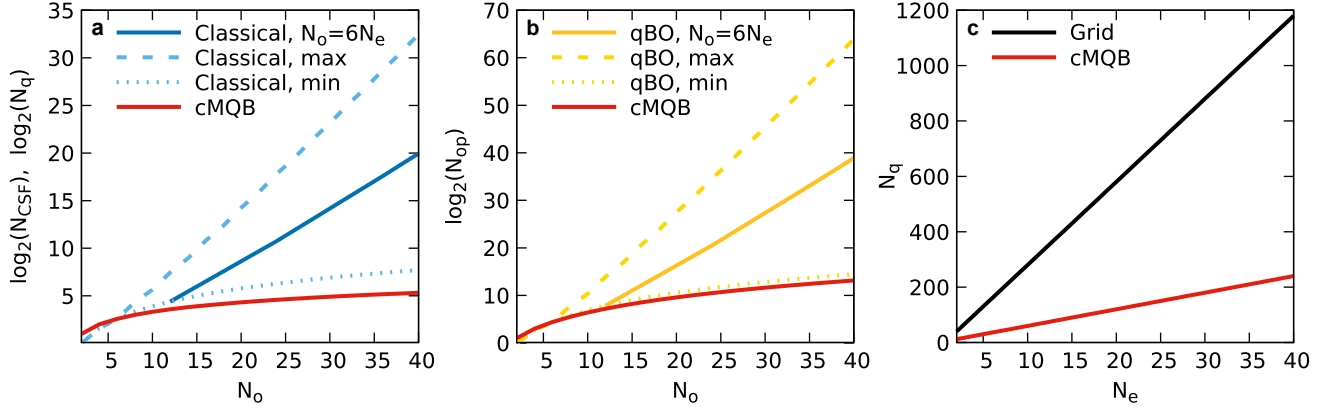


FIG. 4. Resource and computational cost comparison of our cMQB approach with classical and quantum algorithms demonstrating the advantages of cMQB over existing methods. **a**, Resource scaling of electronic degrees of freedom with respect to N_o in a logarithmic scale for classical ($\log_2(N_{\text{CSF}})$) and quantum pre-BO simulations ($\log_2(N_q)$) with singlet electronic states. The resource scaling of our method represented by the red line shows smaller scaling than those of equivalent classical simulations represented by the blue lines for the maximum (dashed), minimum (dotted), and $N_o/N_e = 6$ case (solid) for $N_o > 6$. **b**, Scaling in the number of interactions/gates required to implement the time-evolution operator ($\log(N_{\text{op}})$) with respect to N_o for our cMQB approach (red), and existing quantum algorithms in the BO framework (yellow) labeled as "qBO" for the maximum (dashed), minimum (dotted), and $N_o/N_e = 6$ case (solid). The cMQB approach requires smaller scaling than qBO for $N_o > 6$. **c**, The number of qubits (N_q) required vs. the number of electrons N_e for the pre-BO quantum algorithm proposed in Ref. 34 using grids where $N_q = 3nN_e$ with $n = 10$ (black) and our cMQB approach with $N_q = 6N_e$ (red). Our cMQB method requires smaller number of qubits compared to the previous pre-BO quantum algorithm.

space defines a subset of orbitals for which the exact solution is found, while the remaining (inactive) orbitals have fixed occupations [60]. Only the active orbitals need to be encoded in our simulation because the terms in the Hamiltonian corresponding to inactive orbitals are functions of nuclear coordinates, meaning their effect can be included in the electron integral terms of active orbitals. Likewise, strongly confined modes can be approximately excluded from the nuclear part of the wavefunction for a reduced-dimensional simulation. Together, these reductions in the basis size allow for chemically relevant simulations on near-term quantum hardware.

The simulation cost, which can be measured by the number of interaction terms required, scales as $O(N_o^4 N_{\text{mode}}^k)$ where k is the maximum order of the Taylor expansion for the functions of bosonic degrees of freedom f_I . This cost also remains far smaller than the exponential cost of quantum dynamics simulations on classical computers: $O(N_{\text{CSF}}^2 \prod_{\nu=1}^{N_{\text{mode}}} N_{\nu, \text{bas}}^2)$.

Previous quantum algorithms, including the MQB approach, can potentially have a smaller quantum resource scaling for electronic degrees of freedom than our cMQB method: $\log_2(N_{\text{CSF}}) < N_o$ for the complete CSF basis [37–39] since the CSF space is a subspace of the spin orbital Fock space. However, the simulation cost N_{op} scales as $O(N_{\text{CSF}}^2)$ in the existing quantum simulation approaches, whereas our mapping scales as $O(N_o^4)$ (Fig. 4b). Furthermore, an equivalent approach would require fully diagonalizing the FCI Hamiltonian on a classical computer at a prohibitive cost ($O(N_{\text{CSF}}^3)$), whereas our approach requires only the pre-calculation of electron integrals that scales as $O(N_o^4)$. The GBOA is valid ap-

proximation in many photo-initiated reactions provided that the photon energy absorbed by a system is known so that we can correctly reduce the number of BO states according to that energy window. However, the GBOA breaks down in strong field processes due to the high energy and strong correlation. Furthermore, even if the number of BO states can be reduced, the BO states are obtained by approximate For the nuclear degrees of freedom, our approach has an advantage over other digital or hybrid quantum algorithms for molecular quantum dynamics [37, 38] since our approach has the same resource scaling as the MQB mapping [39] due to the direct mapping on the bosonic modes.

The first proposal of a quantum algorithm for the pre-BO molecular dynamics used a real-space, first quantization representation which has a linear resource scaling with respect to the number of grid points per each degrees of freedom: $nN_{\text{mode}} + 3nN_e$, where n is the number of qubits required for each degree of freedom. The authors suggested a minimum grid size of $n = 10$ [34]. Although their approach also scales linearly with the number of electrons, our approach has a lower resource cost for most molecules with a reasonable basis set size, where $N_{\text{mode}} < N_e$ and $N_o < 30N_e$ (Fig. 4c).

A key approximation in our approach is the exclusion of the Coriolis (rotational-vibrational) coupling from the Hamiltonian. This approximation is not only useful for simplifying the Hamiltonian, but it also comes with an advantage for physical observables. Any observable quantity that depends on the molecular (Eckart) frame is averaged out over the rotational wavefunction, including electronic and nuclear densities. Experimental mea-

surement of these observables in a lab frame results from spontaneous symmetry breaking between the molecule of interest and its environment [61]. This gives a potential advantage for interpretability of our wavefunction compared to other quantum simulation proposals [34, 36]. Furthermore, on the timescale of ultrafast processes (fs-ps), we expect that the effect of Coriolis coupling would be a negligible perturbation on the vibronic states for due to the relatively small rotational frequencies. Future work could explore how this perturbation could be included as an environmental effect without compromising the wavefunction interpretability.

An additional approximation is the lack of relativistic effects, which becomes particularly relevant for heavier atomic nuclei. Classical simulations need to consider additional CSFs with different spin multiplicities to include relativistic effects such as spin-orbit coupling. Therefore the classical resource scaling becomes even larger if intersystem crossing between different multiplicities is included. In contrast, since our pre-BO ansatz spans the entire electronic Fock space for a given spin orbital basis, our approach can describe intersystem crossing by adding spin-orbit coupling terms to the Hamiltonian, without any additional resources required. Based on the form of the vibronic Hamiltonian, our Hamiltonian can be considered as an extended version of electron-phonon coupling models used in the solid state physics field such as the Hubbard-Holstein model [62]. Therefore, our approach can be readily extended to dynamics involving intersystem crossing and translated onto electron-phonon coupling dynamics in solids.

As an analog simulation approach, our approach is subject to environmental noise over the course of the simulation. The noise does not equally affect electronic and vibrational degrees of freedom, since they are encoded in different resources of the simulator. However, because cMQB simulators use bosonic modes to achieve entangling gates, the electronic degrees of freedom are subject to noise on qubit states and bosonic modes. Nonetheless, previous work [39, 63, 64] has shown that controlled noise can be used as an advantage for analog simulators by simulating open quantum systems with a minimal cost. In future work, we will explore noise effects to determine the threshold for a near-term quantum advantage in quantum chemistry.

V. CONCLUSION

In this paper, we proposed an analog quantum simulation approach to simulate the quantum dynamics of vibrations and electrons in molecules. Our approach uses a pre-BO wavefunction ansatz, which converges to the exact solution of the non-relativistic time-dependent Schrödinger equation with increasing electronic basis set size and nuclear Taylor expansion order. Furthermore, our approach can be extended to describe intersystem crossing without additional resources, and can be applied to quantum simulations of electron-phonon coupling models for solids. In contrast, most previously proposed approaches for the simulation of molecular dynamics employ the GBOA, which artificially truncates the electronic state basis. Others used a real-space, first quantization approach, which includes molecular rotations that complicate the interpretability of the wavefunction.

For equivalent descriptions of vibronic dynamics, our approach shows clear scaling advantages over all proposals to date when the quantum resources, number of operations, and number of pre-calculations are considered. This work makes use of existing tools in analog quantum simulation, and model systems such as the example presented in this work can be readily implemented on existing quantum hardware such as trapped ion quantum computers. With improvements in quantum hardware and quantum control, we expect that our approach will demonstrate an early quantum advantage for the simulation of quantum chemistry.

ACKNOWLEDGMENTS

We would like to thank Ting Rei Tan, Ivan Kassal, Seung Kyu Min, and Michael Schuurman for insightful discussion. This research was supported by start-up funding from Dalhousie University, and by National Research Council Canada through the Applied Quantum Challenge program (AQC-100). J.-K.H. was supported by the Basic Science Research Program through the National Research Foundation of Korea funded by the Ministry of Education (RS-2023-00237886).

-
- [1] D. Polli, P. Altoé, O. Weingart, K. M. Spillane, C. Manzoni, D. Brida, G. Tomasello, G. Orlandi, P. Kukura, R. A. Mathies, M. Garavelli, and G. Cerullo, Conical intersection dynamics of the primary photoisomerization event in vision, *Nature* **467**, 440 (2010).
 - [2] S. Gozem, H. L. Luk, I. Schapiro, and M. Olivucci, Theory and Simulation of the Ultrafast Double-Bond Isomerization of Biological Chromophores, *Chem. Rev.* **117**, 13502 (2017).
 - [3] C. Schnedermann, X. Yang, M. Liebel, K. M. Spillane, J. Lugtenburg, I. Fernandez, A. Valentini, I. Schapiro, M. Olivucci, P. Kukura, and R. A. Mathies, Evidence for a vibrational phase-dependent isotope effect on the photochemistry of vision, *Nat. Chem.* **10**, 449 (2018).
 - [4] G. D. Scholes, G. R. Fleming, L. X. Chen, A. Aspuru-Guzik, A. Buchleitner, D. F. Coker, G. S. Engel, R. van Grondelle, A. Ishizaki, D. M. Jonas, J. S. Lundeen, J. K. McCusker, S. Mukamel, J. P. Ogilvie, A. Olaya-Castro, M. A. Ratner, F. C. Spano, K. B. Whaley, and X. Zhu, Using Coherence to Enhance Function in Chemical and

- Biophysical Systems, *Nature* **543**, 647 (2017).
- [5] E. Romero, V. I. Novoderezhkin, and R. van Grondelle, Quantum Design of Photosynthesis for Bio-Inspired Solar-Energy Conversion, *Nature* **543**, 355 (2017).
 - [6] M. Kaucikas, K. Maghlaoui, J. Barber, T. Renger, and J. J. Van Thor, Ultrafast Infrared Observation of Exciton Equilibration from Oriented Single Crystals of Photosystem II, *Nat. Commun.* **7**, 13977 (2016).
 - [7] D. J. Nürnberg, J. Morton, S. Santabarbara, A. Telfer, P. Joliot, L. A. Antonaru, A. V. Ruban, T. Cardona, E. Krausz, A. Boussac, A. Fantuzzi, and A. W. Rutherford, Photochemistry beyond the red limit in chlorophyll f-containing photosystems, *Science* **360**, 1210 (2018).
 - [8] J.-C. Blancon, H. Tsai, W. Nie, C. C. Stoumpos, L. Pedesseau, C. Katan, M. Kepenekian, C. M. M. Soe, K. Appavoo, M. Y. Sfeir, S. Tretiak, P. M. Ajayan, M. G. Kanatzidis, J. Even, J. J. Crochet, and A. D. Mohite, Extremely efficient internal exciton dissociation through edge states in layered 2D perovskites, *Science* **355**, 1288 (2017).
 - [9] S. Nah, B. Spokoyny, C. Stoumpos, C. Soe, M. Kanatzidis, and E. Harel, Spatially Segregated Free-Carrier and Exciton Populations in Individual Lead Halide Perovskite Grains, *Nat. Photonics* **11**, 285 (2017).
 - [10] J. Huang, Y. Yuan, Y. Shao, and Y. Yan, Understanding the Physical Properties of Hybrid Perovskites for Photovoltaic Applications, *Nat. Rev. Mater.* **2**, 17042 (2017).
 - [11] L. Qiao, W.-H. Fang, R. Long, and O. V. Prezhdo, Elimination of Charge Recombination Centers in Metal Halide Perovskites by Strain, *J. Am. Chem. Soc.* **143**, 9982 (2021).
 - [12] Z. Wang, C. Li, and K. Domen, Recent developments in heterogeneous photocatalysts for solar-driven overall water splitting, *Chem. Soc. Rev.* **48**, 2109 (2019).
 - [13] V. K. Singh, C. Yu, S. Badgujar, Y. Kim, Y. Kwon, D. Kim, J. Lee, T. Akhter, G. Thangavel, L. S. Park, J. Lee, P. C. Nandajan, R. Wannemacher, B. n. Milián-Medina, L. Lüer, K. S. Kim, J. Gierschner, and M. S. Kwon, Highly efficient organic photocatalysts discovered via a computer-aided-design strategy for visible-light-driven atom transfer radical polymerization, *Nat. Catal.* **1**, 794 (2018).
 - [14] G. A. Worth and L. S. Cederbaum, Beyond Born-Oppenheimer: Molecular Dynamics Through a Conical Intersection, *Annu. Rev. Phys. Chem.* **55**, 127 (2004).
 - [15] H.-D. Meyer, U. Manthe, and L. Cederbaum, The multi-configurational time-dependent Hartree approach, *Chem. Phys. Lett.* **165**, 73 (1990).
 - [16] R. Crespo-Otero and M. Barbatti, Recent Advances and Perspectives on Nonadiabatic Mixed Quantum-Classical Dynamics, *Chem. Rev.* **118**, 7026 (2018).
 - [17] M. Ben-Nun, J. Quenneville, and T. J. Martínez, Ab Initio Multiple Spawning: Photochemistry from First Principles Quantum Molecular Dynamics, *J. Chem. Phys. A* **104**, 5161 (2000).
 - [18] E. Mátyus, Pre-Born-Oppenheimer molecular structure theory, *Mol. Phys.* **117**, 590 (2019).
 - [19] S. Bubin, M. Pavanello, W.-C. Tung, K. L. Sharkey, and L. Adamowicz, Born-Oppenheimer and Non-Born-Oppenheimer, Atomic and Molecular Calculations with Explicitly Correlated Gaussians, *Chem. Rev.* **113**, 36 (2013).
 - [20] M. Cafiero, S. Bubin, and L. Adamowicz, Non-born-oppenheimer calculations of atoms and molecules, *Phys. Chem. Chem. Phys.* **5**, 1491 (2003).
 - [21] T. Kato and K. Yamanouchi, Time-dependent multi-configuration theory for describing molecular dynamics in diatomic-like molecules, *J. Chem. Phys.* **131**, 164118 (2009).
 - [22] S. Hammes-Schiffer, Nuclear-electronic orbital methods: Foundations and prospects, *J. Chem. Phys.* **155**, 030901 (2021).
 - [23] M. Sibaev, I. Polyak, F. R. Manby, and P. J. Knowles, Molecular second-quantized Hamiltonian: Electron correlation and non-adiabatic coupling treated on an equal footing, *J. Chem. Phys.* **153**, 124102 (2020).
 - [24] S. Sasmal and O. Vendrell, Non-adiabatic quantum dynamics without potential energy surfaces based on second-quantized electrons: Application within the framework of the MCTDH method, *J. Chem. Phys.* **153**, 154110 (2020).
 - [25] S. Lloyd, Universal Quantum Simulators, *Science* **273**, 1073 (1996).
 - [26] S. Wiesner, Simulations of many-body quantum systems by a quantum computer (1996), arXiv:quant-ph/9603028 [quant-ph].
 - [27] C. Zalka, Efficient Simulation of Quantum Systems by Quantum Computers, *Fortschr. Phys.* **46**, 877 (1998).
 - [28] Y. Cao, J. Romero, J. P. Olson, M. Degroote, P. D. Johnson, M. Kieferová, I. D. Kivlichan, T. Menke, B. Peropadre, N. P. D. Sawaya, S. Sim, L. Veis, and A. Aspuru-Guzik, Quantum Chemistry in the Age of Quantum Computing, *Chem. Rev.* **119**, 10856 (2019).
 - [29] A. Peruzzo, J. McClean, P. Shadbolt, M.-H. Yung, X.-Q. Zhou, P. J. Love, A. Aspuru-Guzik, and J. L. O'Brien, A variational eigenvalue solver on a photonic quantum processor, *Nat. Commun.* **5**, 4213 (2014).
 - [30] K. M. Nakanishi, K. Mitarai, and K. Fujii, Subspace-search variational quantum eigensolver for excited states, *Phys. Rev. Res.* **1**, 033062 (2019).
 - [31] P. J. Ollitrault, A. Kandala, C.-F. Chen, P. K. Barkoutsos, A. Mezzacapo, M. Pistola, S. Sheldon, S. Woerner, J. M. Gambetta, and I. Tavernelli, Quantum equation of motion for computing molecular excitation energies on a noisy quantum processor, *Phys. Rev. Res.* **2**, 043140 (2020).
 - [32] S. Yalouz, E. Koridon, B. Senjean, B. Lasorne, F. Buda, and L. Visscher, Analytical Nonadiabatic Couplings and Gradients within the State-Averaged Orbital-Optimized Variational Quantum Eigensolver, *J. Chem. Theory. Comput.* **18**, 776 (2022).
 - [33] S. Tamiya, S. Koh, and Y. O. Nakagawa, Calculating nonadiabatic couplings and Berry's phase by variational quantum eigensolvers, *Phys. Rev. Res.* **3**, 023244 (2021).
 - [34] I. Kassal, S. P. Jordan, P. J. Love, M. Mohseni, and A. Aspuru-Guzik, Polynomial-time quantum algorithm for the simulation of chemical dynamics, *Proc. Natl. Acad. Sci. USA* **105**, 18681 (2008).
 - [35] I. D. Kivlichan, N. Wiebe, R. Babbush, and A. Aspuru-Guzik, Bounding the costs of quantum simulation of many-body physics in real space, *J. Phys. A: Math. Theor.* **50**, 305301 (2017).
 - [36] Y. Su, D. W. Berry, N. Wiebe, N. Rubin, and R. Babbush, Fault-Tolerant Quantum Simulations of Chemistry in First Quantization, *PRX Quantum* **2**, 040332 (2021).
 - [37] P. J. Ollitrault, G. Mazzola, and I. Tavernelli, Nonadiabatic Molecular Quantum Dynamics with Quantum Computers, *Phys. Rev. Lett.* **125**, 260511 (2020).

- [38] P. J. Ollitrault, A. Miessen, and I. Tavernelli, Molecular Quantum Dynamics: A Quantum Computing Perspective, *Acc. of Chem. Res.* **54**, 4229 (2021).
- [39] R. J. MacDonell, C. E. Dickerson, C. J. T. Birch, A. Kumar, C. L. Edmunds, M. J. Biercuk, C. Hempel, and I. Kassal, Analog quantum simulation of chemical dynamics, *Chem. Sci.* **12**, 9794 (2021).
- [40] R. J. MacDonell, T. Navickas, T. F. Wohlers-Reichel, C. H. Valahu, A. D. Rao, M. J. Millican, M. A. Curring-ton, M. J. Biercuk, T. R. Tan, C. Hempel, and I. Kassal, Predicting molecular vibronic spectra using time-domain analog quantum simulation, *Chem. Sci.* **14**, 9439 (2023).
- [41] C. H. Valahu, V. C. Olaya-Agudelo, R. J. MacDonell, T. Navickas, A. D. Rao, M. J. Millican, J. B. Pérez-Sánchez, J. Yuen-Zhou, M. J. Biercuk, C. Hempel, T. R. Tan, and I. Kassal, Direct observation of geometric-phase interference in dynamics around a conical intersection, *Nat. Chem.* **15**, 1503 (2023).
- [42] A. Kovyshin, M. Skogh, A. Broo, S. Mensa, E. Sahin, J. Crain, and I. Tavernelli, A quantum computing implementation of nuclearelectronic orbital (NEO) theory: Toward an exact pre-Born-Oppenheimer formulation of molecular quantum systems, *J. Chem. Phys.* **158**, 214119 (2023).
- [43] P. Bunker and P. Jensen, *Molecular Symmetry and Spectroscopy*, 2nd Ed. (NRC Research Press, Ottawa, 2006).
- [44] J. Kim, K. Hong, S. Choi, S.-Y. Hwanga, and W. Y. Kim, Configuration interaction singles based on the real-space numerical grid method: Kohn-Sham versus Hartree-Fock orbitals, *Phys. Chem. Chem. Phys.* **17**, 31434 (2015).
- [45] C. A. Mead and D. G. Truhlar, Conditions for the definition of a strictly diabatic electronic basis for molecular systems, *J. Chem. Phys.* **77**, 6090 (1982).
- [46] D. R. Yarkony, C. Xie, X. Zhu, Y. Wang, C. L. Malbon, and H. Guo, Diabatic and adiabatic representations: Electronic structure caveats, *Comput. Theor. Chem.* **1152**, 41 (2019).
- [47] J. Argüello-Luengo, A. González-Tudela, T. Shi, P. Zoller, and J. I. Cirac, Analogue quantum chemistry simulation, *Nature* **574**, 215 (2019).
- [48] T. Hartke, B. Oreg, N. Jia, and M. Zwierlein, Quantum register of fermion pairs, *Nature* **601**, 537 (2022).
- [49] P. Jordan and E. Wigner, Über das paulische äquivalenzverbot, *Z. Phys.* **47**, 631 (1928).
- [50] S. B. Bravyi and A. Y. Kitaev, Fermionic Quantum Computation, *Ann. Phys.* **298**, 210 (2002).
- [51] N. Hatano and M. Suzuki, Finding exponential product formulas of higher orders, in *Quantum Annealing and Other Optimization Methods*, edited by A. Das and B. K. Chakrabarti (Springer Berlin Heidelberg, Berlin, Heidelberg, 2005) pp. 37–68.
- [52] L. Lamata, A. Mezzacapo, J. Casanova, and E. Solano, Efficient quantum simulation of fermionic and bosonic models in trapped ions, *EPJ Quantum Technol.* **1**, 9 (2014).
- [53] O. Katz, M. Cetina, and C. Monroe, Programmable N -Body Interactions with Trapped Ions, *PRX Quantum* **4**, 030311 (2023).
- [54] R. Cleve, A. Ekert, C. Macchiavello, and M. Mosca, Quantum algorithms revisited, *Proc. Roy. Soc. A* **454**, 339 (1998).
- [55] C. Flühmann and J. P. Home, Direct Characteristic-Function Tomography of Quantum States of the Trapped-Ion Motional Oscillator, *Phys. Rev. Lett.* **125**, 043602 (2020).
- [56] S. Shin and H. Metiu, Nonadiabatic effects on the charge transfer rate constant: A numerical study of a simple model system, *J. Chem. Phys.* **102**, 9285 (1995).
- [57] Y. Suzuki and K. Yamashita, Real-time electron dynamics simulation of two-electron transfer reactions induced by nuclear motion, *Chem. Phys. Lett.* **531**, 216 (2012).
- [58] J. Johansson, P. Nation, and F. Nori, QuTiP 2: A Python framework for the dynamics of open quantum systems, *Comput. Phys. Commun.* **184**, 1234 (2013).
- [59] K. Mølmer and A. Sørensen, Multiparticle Entanglement of Hot Trapped Ions, *Phys. Rev. Lett.* **82**, 1835 (1999).
- [60] B. O. Roos, P. R. Taylor, and P. E. Sigbahn, A complete active space SCF method (CASSCF) using a density matrix formulated super-CI approach, *Chem. Phys.* **48**, 157 (1980).
- [61] E. Mátyus and P. Cassam-Chenaï, Orientational decoherence within molecules and emergence of the molecular shape, *J. Chem. Phys.* **154**, 024114 (2021).
- [62] E. Berger, P. Valášek, and W. von der Linden, Two-dimensional Hubbard-Holstein model, *Phys. Rev. B* **52**, 4806 (1995).
- [63] V. C. Olaya-Agudelo, B. Stewart, C. H. Valahu, R. J. MacDonell, M. J. Millican, V. G. Matsos, F. Scucimarra, T. R. Tan, and I. Kassal, Simulating open-system molecular dynamics on analog quantum computers, *arXiv [quant-ph]:2407.17819* (2024).
- [64] K. Sun, M. Kang, H. Nuomin, G. Schwartz, D. N. Beratan, K. R. Brown, and J. Kim, Quantum Simulation of Spin-Boson Models with Structured Bath, *arXiv [quant-ph]:2405.14624* (2024).

Supplemental Material for “Analog Quantum Simulation of Coupled Electron-Nuclear Dynamics in Molecules”

Jong-Kwon Ha¹ and Ryan J. MacDonell^{1, 2, *}

¹*Department of Chemistry, Dalhousie University,
6243 Alumni Cres, Halifax, NS B3H 4R2, Canada*

²*Department of Physics and Atmospheric Science, Dalhousie University,
1453 Lord Dalhousie Dr, Halifax, NS B3H 4R2, Canada*

(Dated: September 9, 2024)

I. ELECTRON INTEGRALS

The electron integral terms in Eq. 3 (one- and two-electron integrals, and the first and second order orbital derivative couplings) depend on the normal mode coordinates and are given by

$$h_{pq}(\mathbf{Q}) = \int d\mathbf{r} \phi_p^*(\mathbf{r}; \mathbf{Q}) \left(-\frac{\nabla^2}{2} + v_{\text{en}}(\mathbf{r}, \mathbf{Q}) \right) \phi_q(\mathbf{r}; \mathbf{Q}), \quad (\text{S1})$$

$$v_{pqrs}(\mathbf{Q}) = \int d\mathbf{r} \int d\mathbf{r}' \phi_p^*(\mathbf{r}; \mathbf{Q}) \phi_q^*(\mathbf{r}'; \mathbf{Q}) \frac{1}{|\mathbf{r} - \mathbf{r}'|} \phi_r(\mathbf{r}; \mathbf{Q}) \phi_s(\mathbf{r}'; \mathbf{Q}), \quad (\text{S2})$$

$$d_{\nu,pq}(\mathbf{Q}) = \delta_{\sigma_p \sigma_q} \int d\mathbf{r} \phi_p^*(\mathbf{r}; \mathbf{Q}) \frac{\partial}{\partial Q_\nu} \phi_q(\mathbf{r}; \mathbf{Q}), \quad (\text{S3})$$

$$g_{\nu,pq}(\mathbf{Q}) = \delta_{\sigma_p \sigma_q} \int d\mathbf{r} \phi_p^*(\mathbf{r}; \mathbf{Q}) \frac{\partial^2}{\partial Q_\nu^2} \phi_q(\mathbf{r}; \mathbf{Q}). \quad (\text{S4})$$

The electron-nuclear potential $v_{\text{en}}(\mathbf{r}, \mathbf{Q})$ and the nuclear-nuclear potential $V_{\text{nn}}(\mathbf{Q})$ are given in terms of Cartesian nuclear positions \mathbf{R}_α for nucleus α ,

$$v_{\text{en}}(\mathbf{r}, \mathbf{Q}) = -\sum_{\alpha} \frac{Z_{\alpha}}{|\mathbf{r} - \mathbf{R}_{\alpha}|}, \quad (\text{S5})$$

$$V_{\text{nn}}(\mathbf{Q}) = \sum_{\alpha\beta} \frac{Z_{\alpha} Z_{\beta}}{|\mathbf{R}_{\alpha} - \mathbf{R}_{\beta}|}, \quad (\text{S6})$$

where Z_{α} is the charge of nucleus α . The nuclear internal coordinates and the vector of all Cartesian coordinates are related by a unitary transformation.

II. TWO-ELECTRON SHIN-METIU MODEL HAMILTONIAN

The one-dimensional, two-electron Shin-Metiu model Hamiltonian has two fixed ions, a moving ion between them, and two electrons in one-dimensional space [1, 2]:

$$\hat{H}(r_1, r_2, R) = -\frac{1}{2M} \frac{\partial^2}{\partial R^2} + V_{\text{nn}}(R) + \hat{h}_{1e}(r_1, R) + \hat{h}_{1e}(r_2, R) + v_{\text{ee}}(r_1, r_2). \quad (\text{S7})$$

Here, r_i represents the position of the electron i , R is the position of the moving, and $M = 1836.0$ a.u. is the mass of the moving ion. In the above equation, we replaced the original Coulomb repulsion exerted on the moving ion by the fixed ions by a harmonic potential,

$$V_{\text{nn}}(R) = \frac{1}{2} k R^2, \quad (\text{S8})$$

* rymac@dal.ca

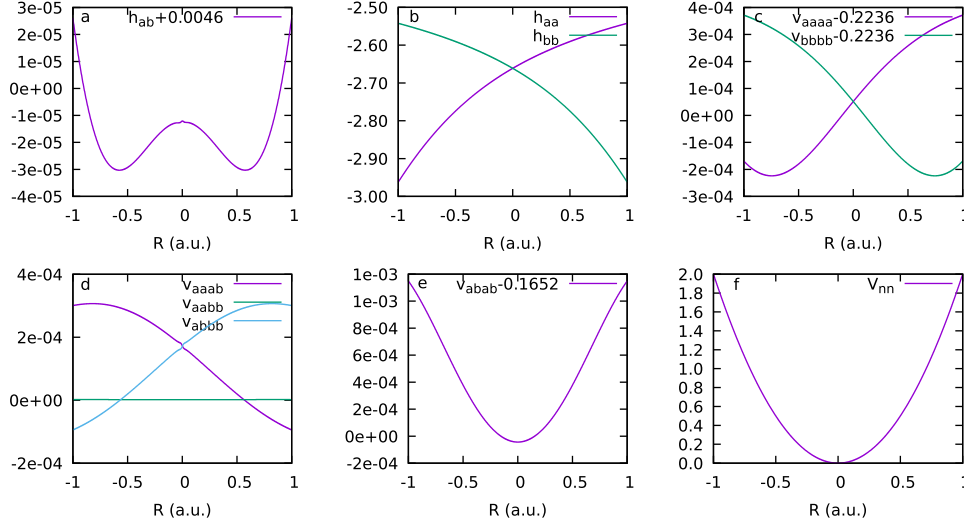


FIG. S1. The one-/two-electron integrals and the nuclear bound potential. **a-b**, one-electron integrals h'_{pq} s. **c-e**, two-electron integrals v'_{pqrs} s. **f**, nuclear bound potential V_{nn} .

with a spring constant $k = 4.0$ a.u. The one-electron Hamiltonian \hat{h}_{1e} [1] is defined as

$$\hat{h}_{1e}(r, R) = -\frac{1}{2} \frac{\partial^2}{\partial r^2} - \frac{\text{erf}\left(\frac{|R-r|}{C_c}\right)}{|R-r|} - \frac{\text{erf}\left(\frac{|r-\frac{L}{2}|}{C_r}\right)}{|r-\frac{L}{2}|} - \frac{\text{erf}\left(\frac{|r+\frac{L}{2}|}{C_l}\right)}{|r+\frac{L}{2}|}, \quad (\text{S9})$$

and the electron-electron interaction [2] is given by

$$v_{ee}(r_1, r_2) = \frac{\text{erf}\left(\frac{|r_1-r_2|}{C_e}\right)}{|r_1-r_2|}, \quad (\text{S10})$$

where $L = 5.4$ a.u. is the distance between fixed ions. $C_l = C_r = 0.3$ a.u., and $C_c = 0.6$ a.u. are soft Coulomb parameters for the fixed ions and the moving ion, respectively, and $C_e = 5.0$ a.u. is a soft Coulomb parameter for electron-electron repulsion. The origin is set to the mid-point of the two fixed ions. All parameters in the model Hamiltonian are chosen such that the model dynamics show an oscillation in the occupation numbers of spin-orbitals within the time range of 2500 a.u. to exhibit a vibronic effect, while keeping the Taylor expansion order for electron integrals and nuclear basis set small for a feasible classical simulation.

We selected the two diabatic orbitals φ_a and φ_b with spin-up and spin-down configurations as a spin-orbital basis set, obtained from two adiabatic orbitals ψ_l , the eigenstates of the Schrödinger equation $\hat{h}_{1e}\psi_l = e_l\psi_l$ for the one-electron Shin-Metiu model [1]. The electron integrals of the diabatic orbitals and the nuclear bound potential are shown in Fig. S1.

TABLE S1. Taylor expansion coefficients of the nuclear position R for the electron integrals

| $v(R) \approx v_0 + v_1 R$ | h_{aa} | h_{bb} | h_{ab} | v_{aaaa} | v_{bbbb} | v_{abab} | v_{aabb} | v_{abbb} | v_{aabb} |
|----------------------------|----------|----------|----------|------------|------------|------------|------------|------------|------------|
| v_0 | -2.66 | -2.66 | -0.0046 | 0.2236 | 0.2236 | 0.1652 | 0.0001 | 0.0001 | 0.0000015 |
| v_1 | 0.2 | -0.2 | 0.0 | 0.00044 | -0.00044 | 0.0 | 0.0 | 0.0 | 0.0 |

III. HAMILTONIAN MAPPING

As a result of the Jordan-Wigner mapping with the four spin orbitals, the two-electron Shin-Metiu model Hamiltonian is mapped to

$$\begin{aligned}
\hat{H}_{\text{mol}} = & -\frac{1}{2M} \frac{\partial^2}{\partial R^2} + \frac{1}{2} k R^2 + h_{aa} + h_{bb} + \frac{1}{4} (v_{aaaa} + v_{bbbb} + 4v_{abab} - 2v_{aabb}) \\
& - \left(\frac{h_{aa}}{2} + \frac{1}{4} (v_{aaaa} + 2v_{abab} - v_{aabb}) \right) (\hat{Z}_1 + \hat{Z}_2) - \left(\frac{h_{bb}}{2} + \frac{1}{4} (v_{bbbb} + 2v_{abab} - v_{aabb}) \right) (\hat{Z}_3 + \hat{Z}_4) \\
& + \frac{1}{4} v_{aaaa} \hat{Z}_1 \hat{Z}_2 + \frac{1}{4} v_{bbbb} \hat{Z}_3 \hat{Z}_4 + \frac{1}{4} v_{abab} (\hat{Z}_1 \hat{Z}_4 + \hat{Z}_2 \hat{Z}_3) + \frac{1}{4} (v_{abab} - v_{aabb}) (\hat{Z}_1 \hat{Z}_3 + \hat{Z}_2 \hat{Z}_4) \\
& + \left(\frac{h_{ab}}{2} + \frac{1}{4} (v_{aaab} + v_{abbb}) \right) (\hat{X}_1 \hat{Z}_2 \hat{X}_3 + \hat{Y}_1 \hat{Z}_2 \hat{Y}_3 + \hat{X}_2 \hat{Z}_3 \hat{X}_4 + \hat{Y}_2 \hat{Z}_3 \hat{Y}_4) \\
& - \frac{1}{4} v_{aaab} (\hat{Z}_1 \hat{X}_2 \hat{Z}_3 \hat{X}_4 + \hat{Z}_1 \hat{Y}_2 \hat{Z}_3 \hat{Y}_4 + \hat{X}_1 \hat{X}_3 + \hat{Y}_1 \hat{Y}_3) - \frac{1}{4} v_{abbb} (\hat{X}_1 \hat{Z}_2 \hat{X}_3 \hat{Z}_4 + \hat{Y}_1 \hat{Z}_2 \hat{Y}_3 \hat{Z}_4 + \hat{X}_2 \hat{X}_4 + \hat{Y}_2 \hat{Y}_4) \\
& - \frac{1}{4} v_{aabb} (\hat{X}_1 \hat{X}_2 \hat{Y}_3 \hat{Y}_4 + \hat{Y}_1 \hat{Y}_2 \hat{X}_3 \hat{X}_4 - \hat{X}_1 \hat{Y}_2 \hat{Y}_3 \hat{X}_4 - \hat{Y}_1 \hat{X}_2 \hat{X}_3 \hat{Y}_4).
\end{aligned} \tag{S11}$$

The diabatic orbitals (Fig. S1a and S1b) are very localized and not significantly changed by the nuclear motion due to the strong nonadiabatic character of the model system with the chosen parameters [1]. The magnitude of changes in some integrals is also small. Therefore, we can approximate the electron integrals of diabatic orbitals up to the first order Taylor expansion of the nuclear position ($v(R) \approx v_0 + v_1 R$) where $R = Q/\sqrt{M}$, and $\hat{Q} = (\hat{b}^\dagger + \hat{b})/\sqrt{2}$ with ladder operators \hat{b}^\dagger and \hat{b} of our single mode. The expansion coefficients for the electron integrals are given in Tab. S1.

As a result, the final coupled multi-qubit-boson (cMQB) Hamiltonian used for the dynamics can be written as

$$\begin{aligned}
\hat{H}_{\text{cMQB}} = & \omega \hat{b}^\dagger \hat{b} + V_0^0 + V_1^0 (\hat{b} + \hat{b}^\dagger) + \left(V_0^1 + V_1^1 (\hat{b} + \hat{b}^\dagger) \right) (\hat{Z}_1 + \hat{Z}_2) + \left(V_0^2 + V_1^2 (\hat{b} + \hat{b}^\dagger) \right) (\hat{Z}_3 + \hat{Z}_4) \\
& + \left(V_0^3 + V_1^3 (\hat{b} + \hat{b}^\dagger) \right) \hat{Z}_1 \hat{Z}_2 + \left(V_0^4 + V_1^4 (\hat{b} + \hat{b}^\dagger) \right) \hat{Z}_3 \hat{Z}_4 \\
& + \left(V_0^5 + V_1^5 (\hat{b} + \hat{b}^\dagger) \right) (\hat{Z}_1 \hat{Z}_4 + \hat{Z}_2 \hat{Z}_3) + \left(V_0^6 + V_1^6 (\hat{b} + \hat{b}^\dagger) \right) (\hat{Z}_1 \hat{Z}_3 + \hat{Z}_2 \hat{Z}_4) \\
& + \left(V_0^7 + V_1^7 (\hat{b} + \hat{b}^\dagger) \right) (\hat{X}_1 \hat{Z}_2 \hat{X}_3 + \hat{Y}_1 \hat{Z}_2 \hat{Y}_3 + \hat{X}_2 \hat{Z}_3 \hat{X}_4 + \hat{Y}_2 \hat{Z}_3 \hat{Y}_4) \\
& + \left(V_0^8 + V_1^8 (\hat{b} + \hat{b}^\dagger) \right) (\hat{Z}_1 \hat{X}_2 \hat{Z}_3 \hat{X}_4 + \hat{Z}_1 \hat{Y}_2 \hat{Z}_3 \hat{Y}_4 + \hat{X}_1 \hat{X}_3 + \hat{Y}_1 \hat{Y}_3) \\
& + \left(V_0^9 + V_1^9 (\hat{b} + \hat{b}^\dagger) \right) (\hat{X}_1 \hat{Z}_2 \hat{X}_3 \hat{Z}_4 + \hat{Y}_1 \hat{Z}_2 \hat{Y}_3 \hat{Z}_4 + \hat{X}_2 \hat{X}_4 + \hat{Y}_2 \hat{Y}_4) \\
& + \left(V_0^{10} + V_1^{10} (\hat{b} + \hat{b}^\dagger) \right) (\hat{X}_1 \hat{X}_2 \hat{Y}_3 \hat{Y}_4 + \hat{Y}_1 \hat{Y}_2 \hat{X}_3 \hat{X}_4 - \hat{X}_1 \hat{Y}_2 \hat{Y}_3 \hat{X}_4 - \hat{Y}_1 \hat{X}_2 \hat{X}_3 \hat{Y}_4),
\end{aligned} \tag{S12}$$

where $\omega = \sqrt{k/M}$ and V_i^I corresponds to the i -th order net expansion coefficients of Q for the I -th group of Pauli strings.

IV. COUPLED MULTI-QUBIT-BOSON SIMULATION

For the dynamics simulation and the calculation of the density shown in Fig. 3, we used 20 harmonic oscillator eigenfunctions as a bosonic basis set.

The time evolution of the fractional occupation number (FON) of ϕ_1 , i.e. the spin-up configuration of the diabatic orbital φ_a , is shown in Fig. S2a with different Trotter steps Δt . We can see the change of FON which indicates the electron transfer between fixed ions, since the orbitals are localized to the ions.

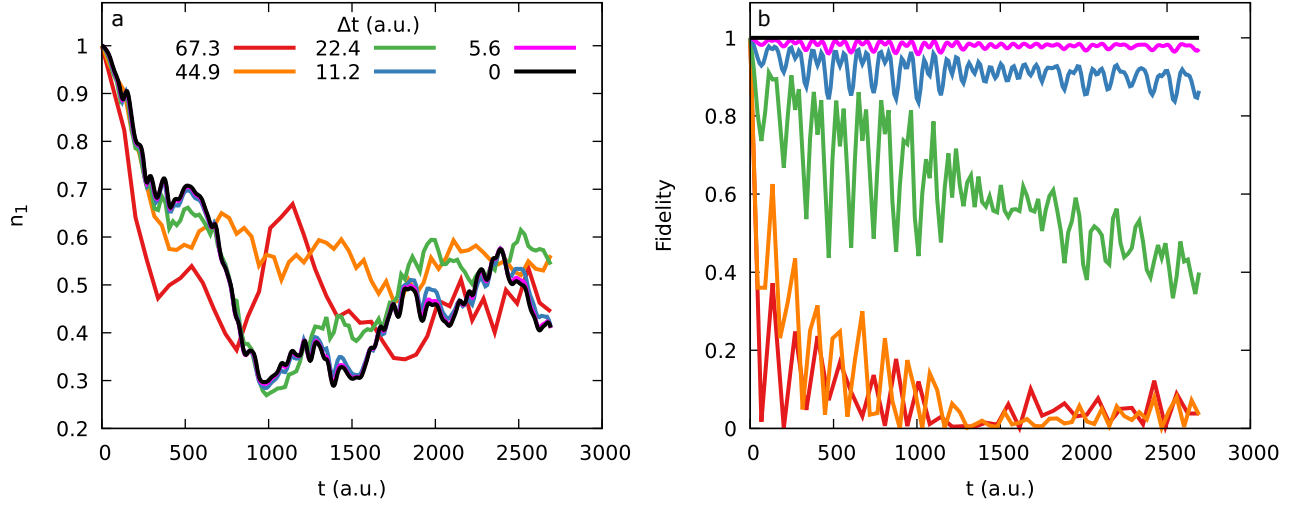


FIG. S2. Time-evolution of orbital occupation number and fidelity. The black line ($\Delta t = 0$) represents the exact result without Trotterization. **a**, the orbital occupation number $\langle \Psi | \hat{a}_1^\dagger \hat{a}_1 | \Psi \rangle$. **b**, the fidelity with different Trotter steps Δt .

Fig. S2b shows the fidelity $|\langle \Psi | \Psi_{\text{exact}} \rangle|^2$ which indicates how exact the state $|\Psi\rangle$, the vibronic state propagated with Trotterization. The Trotter step converges approximately to the exact result at $\Delta t = 5.6$ a.u. ≈ 0.1 fs which is a reasonable time scale often used for traditional NAMD simulations. We can estimate the Trotter step size of an actual quantum simulation on a cMQB device from the ratio between time scales of molecular vibronic dynamics and the natural frequency of bosonic degrees of freedom in the cMQB device, which gives us $\Delta t \sim 0.1 \mu\text{s}$ and ~ 0.1 ps for trapped ions and cQED, respectively.

We performed the cMQB simulation using the QuTiP package [3] in Python.

V. BORN-OPPENHEIMER FRAMEWORK SIMULATION

We can construct a full configuration interaction (FCI) space with three singlet configuration state functions (CSFs) for two electrons in four restricted spin orbitals, i.e. two closed shell configurations and one open-shell configurations:

$$|\Phi_1^{\text{CSF}}\rangle = |1100\rangle, \quad (\text{S13})$$

$$|\Phi_2^{\text{CSF}}\rangle = |0011\rangle, \quad (\text{S14})$$

$$|\Phi_3^{\text{CSF}}\rangle = \frac{1}{\sqrt{2}}(|1001\rangle - |0110\rangle). \quad (\text{S15})$$

The corresponding electronic Hamiltonian matrix in the CSF basis is,

$$H_{\text{el}}^{\text{CSF}} = \begin{pmatrix} 2h_{aa} + v_{aaaa} & v_{aabb} & \sqrt{2}(h_{ab} + v_{aaab}) \\ v_{aabb} & 2h_{bb} + v_{bbbb} & \sqrt{2}(h_{ab} + v_{bbba}) \\ \sqrt{2}(h_{ab} + v_{aaab}) & \sqrt{2}(h_{ab} + v_{bbba}) & h_{aa} + h_{bb} + v_{abab} + v_{aabb} \end{pmatrix}. \quad (\text{S16})$$

Because all orbital derivative couplings are zero in our model, the CSF basis itself is also a diabatic basis for the two-electron state. We obtain a Born-Oppenheimer (BO) basis set by diagonalizing the CSF Hamiltonian with a unitary transformation:

$$\Phi_j^{\text{BO}}(r_1, r_2; R) = \sum_i \Phi_i^{\text{CSF}}(r_1, r_2; R) U_{ij}(R). \quad (\text{S17})$$

The joint electron-nuclear density function $\rho(r, R)$ of a two-electron state $\Phi(r_1, r_2; R)$ can be calculated as $2 \int dr_1 \int dr_2 \delta(r - r_1) |\Phi(r_1, r_2; R)|^2$. The joint density functions of CSF states and BO states are shown in Fig. S3 and S4, respectively. The electrons are localized around the left and right fixed ions for $|\Phi_1^{\text{CSF}}\rangle$ and $|\Phi_2^{\text{CSF}}\rangle$, respectively, while the open-shell singlet configuration $|\Phi_3^{\text{CSF}}\rangle$ shows electron densities on the both side of the fixed ions. The BO states show mixed

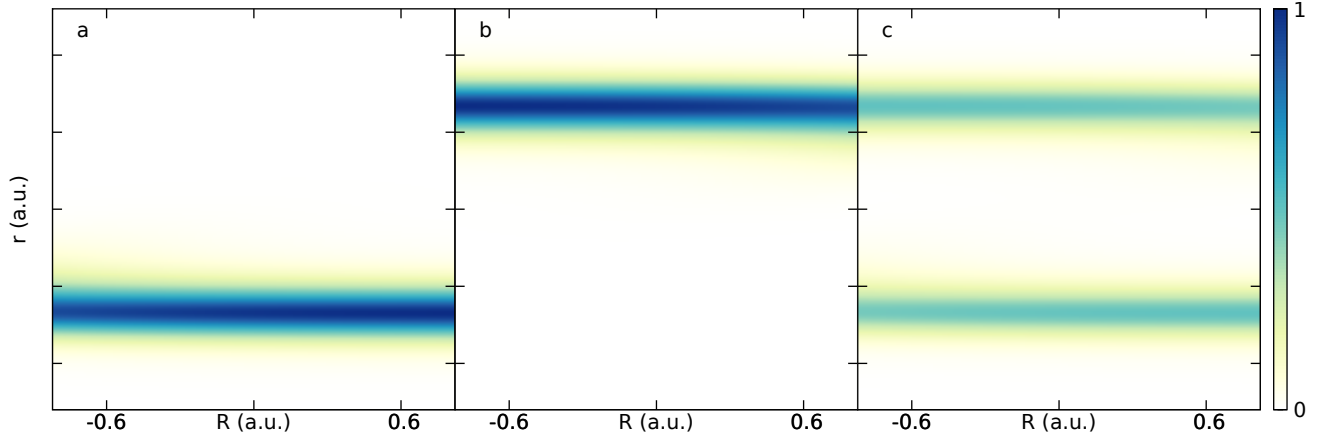


FIG. S3. The density function $\rho(r, R)$ for CSF states. **a**, $|\Phi_1^{\text{CSF}}\rangle$, **b**, $|\Phi_2^{\text{CSF}}\rangle$, and **c**, $|\Phi_3^{\text{CSF}}\rangle$.

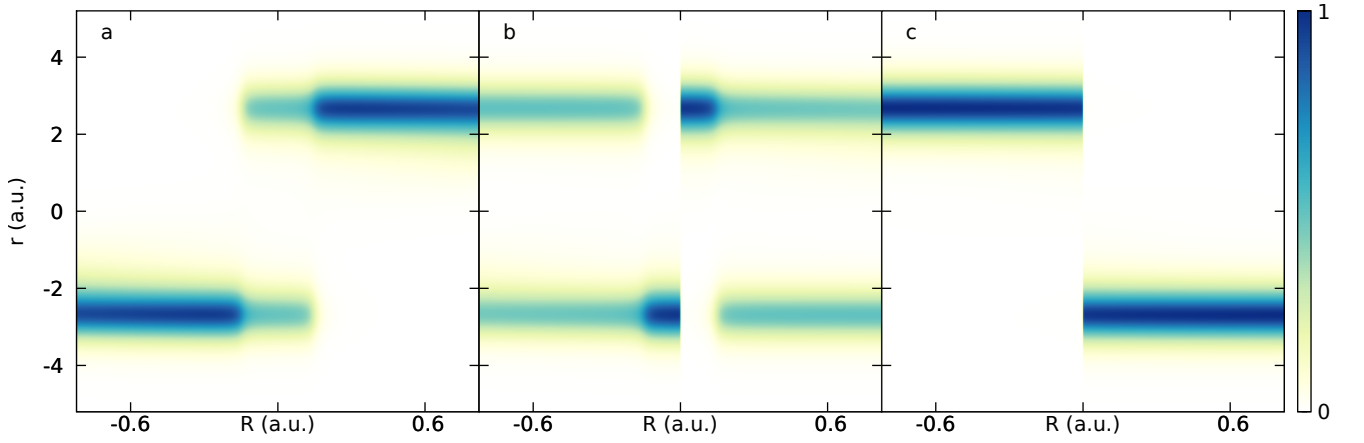


FIG. S4. The density function $\rho(r, R)$ for BO states: **a** $|\Phi_1^{\text{BO}}\rangle$, **b** $|\Phi_2^{\text{BO}}\rangle$, and **c** $|\Phi_3^{\text{BO}}\rangle$.

character across the nuclear with a drastic change from one closed shell to the other closed shell at the origin for $|\Phi_2^{\text{BO}}\rangle$ and $|\Phi_3^{\text{BO}}\rangle$ indicating the strong nonadiabatic coupling (NAC) between them, while the coupling between $|\Phi_1^{\text{BO}}\rangle$ and $|\Phi_2^{\text{BO}}\rangle$ is relatively small. The diagonal CSF Hamiltonian matrix elements and the BO potential energy surfaces with nonadiabatic couplings (NACs) between BO states, $D_{ij} = \langle \Phi_i^{\text{BO}} | \frac{\partial}{\partial R} \Phi_j^{\text{BO}} \rangle$ using the coefficients in Tab. S1 are plotted in Fig. S5.

We performed the equivalent dynamics in the BO representation using the Born-Huaing expansion (Eq. 8), where the effective Hamiltonian in the BO representation for time-dependent Schrödinger equation can be found in Ref. 4. For the GBOA, the ground state $|\Phi_1^{\text{BO}}\rangle$ is neglected since it has a relatively small NAC with the excited states compared to the NAC between the first and second excited states.

We used sinc discrete variable representation (DVR) for the nuclear basis set on 1500 uniform grid points from $R = -1.0$ to 1.0 a.u. and the initial state is prepared in the BO representation via the unitary transformation between the CSF and BO basis set (Eq. S17) on the nuclear grid. Since the initial electronic state which corresponds to $|\Phi_1^{\text{CSF}}\rangle$ has negligible contribution on the BO ground state, the GBOA basis reproduces an accurate initial state. We propagated the wavefunction using a time-evolution matrix by direct exponentiation of DVR Hamiltonian matrix in the BO representation.

We performed the BO framework simulation using the QuTiP package [3] in Python.

[1] S. Shin and H. Metiu, Nonadiabatic effects on the charge transfer rate constant: A numerical study of a simple model system, J. Chem. Phys. **102**, 9285 (1995).

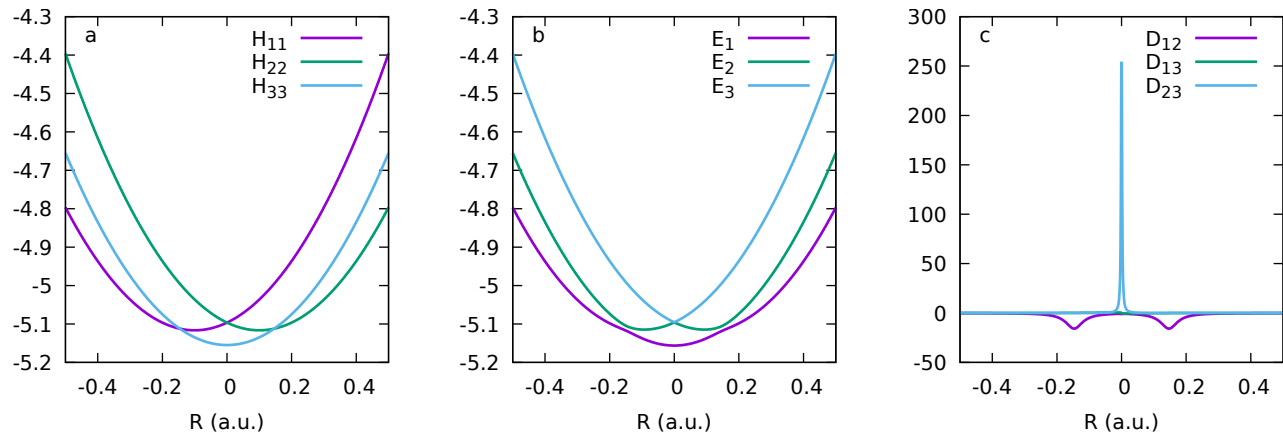


FIG. S5. **a**, The diagonal CSF Hamiltonian matrix elements, **b**, the BO potential energy surfaces, and **c**, the NACs between BO states.

- [2] Y. Suzuki and K. Yamashita, Real-time electron dynamics simulation of two-electron transfer reactions induced by nuclear motion, *Chem. Phys. Lett.* **531**, 216 (2012).
- [3] J. Johansson, P. Nation, and F. Nori, QuTiP 2: A Python framework for the dynamics of open quantum systems, *Comput. Phys. Commun.* **184**, 1234 (2013).
- [4] G. A. Worth and L. S. Cederbaum, Beyond Born-Oppenheimer: Molecular Dynamics Through a Conical Intersection, *Annu. Rev. Phys. Chem.* **55**, 127 (2004).